TRIESTE RECONSTRUCTION SOFTWARE FOR COMPASS RICH 1

Progress Report - December '99.

P. Schiavon

1 INTRODUCTION

The TRIESTE pattern recognition method for the identification of *rings* in the COMPASS RICH 1, has already been described in some COMPASS Internal Notes by P. Schiavon, available on the COMPASS Web page (**'Studies of the Cerenkov emission angle reconstruction Part 1'** (10/6/97) and **'Part 2'** (27/10/97), **'Pattern recognition for COMPASS RICH 1'** Progress Report (8/5/99)), to which we refer.

Let's only remind that the reconstruction line can be divided into two steps :

a) the **recognition** of a *ring*, associated to a measured particle trajectory, together with the determination of its relevant parameters, mainly the Cerenkov emission angle θ_C;
To this purpose the trajectories of the particles which enter the RICH are expected to be measured with good accuracy; in particular the position and the direction of the particle trajectory at (or extrapolated to) the RICH entrance window and the position of the particle trajectory at (or extrapolated to) the exit window are needed.
An approximate knowledge of the momentum of the particle is useful for some corrections in the procedure.
To reconstruct the *ring* the active pad positions on the RICH photon chambers are used, together with the pad Pulse Heights (PH); let remind that a clustering procedure is used to better estimate the photon impact points.

b) the **identification** of the mass m of the particle for which a *ring* has been reconstructed.
To this purpose the particle momentum p has to be well measured.

The focus is on step 1, step 2 being at present in a less advanced stage.

The studies on which we report, are essentially MonteCarlo studies, in which both the incoming muon beam with its interactions and the RICH behaviour in all its parts are fully simulated.

2 SIMULATION

a) Beam.

The simulated beam is a 100. GeV/c momentum μ^+ beam. Its phase-space is taken from the Lau Gatignon MonteCarlo studies. $\mu's$ passing through the PT material are forced to interact according to LEPTO generator features.
All the typical effects (multiple Coulomb scattering, energy losses, decays, e.m. and hadronic interactions, δ-ray emission, ...) are taken into account for all the particles produced in the interactions.

Note that independent MC data files, again based on the Lau Gatignon MonteCarlo, have been generated to simulate the beam 'far' halo (defined as $\mu's$ which cross some beam tranport element) to study the μ background conditions expected because of the photon chamber memory time. Note also that essentially all of the beam not interacting in the target goes through the beam pipe inside the RICH volume and then does not radiate. This study is still ongoing and no results will be discussed in the present report.

b) Experimental setup.

Particles are tracked through the PT material and magnetic field and all the elements of the first spectrometer and RICH 1 in the present configuration.

c) RICH.

The geometry and the behaviour of all the parts of the RICH are fully taken into account. In particular, in the Cerenkov photon emission, the correct photon energy spectrum is used. Moreover the response of the photon chambers (4 upper and 4 lower) takes advantage of the experimental results obtained from the test beam data.
At present are still missing in the simulation :
- the mirror element geometry; at present two one piece (upper and lower) spherical mirrors are used instead of two arrays of mirror elements of hexagonal (or similar) shape; then differences in mirror element radii and positioning, as well as dead zones among them, are not taken into account in this report. This is a point of major relevance for the RICH response, but the gross features of the effect have already been evaluated in a separate analysis (see the COMPASS note **'Studies of the effect of mirror radius value ...'** (8/6/97) by P. Schiavon, on the COMPASS Web page and **'Studies of the optics of COMPASS RICH'**, Proceedings of RICH98, 15-20 September 1998).
- some minor details of the photon chambers, like the gaps among adjacent pads (the pitch is correct).
- the photon absorbtion in the C_4F_{10} radiator (gas) and the corrections to its refraction index due to gravity effects.
- the material of the pipe around the through passing beam region (at present this region is only kept not active for Cerenkov emission).

3 RESOLUTION IN CERENKOV EMISSION ANGLE

a) Definition.

The resolution of the method in the reconstructed Cerenkov emission angle (θ_{rec}^{ring}) has been evaluated using the MC data.
A value of θ_{MC}^{ring} is computed for each particle from its momentum and mass, as known from MC generation and compared with θ_{rec}^{ring}, the reconstructed emission angle.
The width of the distribution $\Delta\theta = \theta_{rec}^{ring}$ - θ_{MC}^{ring} is then evaluated as a function of some kinematical variable as the β of the particle or its momentum p.

b) Calibration with MC events.

In fig.1 $\Delta\theta$ (mrad) is plotted as a function of the (calculated) particle β, in the range $0.9984 \leq \beta < 1.$, in 8 bins of $\Delta\beta = 0.0002$.
Note that with the radiator used (C_4F_{10}, $n = 1.00153$) the threshold for Cerenkov emission is at $\beta = 0.99847$.
The increasing in σ_{θ}^{ring} as β decreases from 1. dowmwards is quite evident, as well as the offset in the mean value, θ_{off}.
In fig.2 (a) σ_{θ}^{ring} (mrad) (as result of a gaussian fit to the distributions of fig.1) is plotted as a function of β, with superimposed a fit of a function of the form : $f(\beta) = a$ / $(\beta$ - $b)^c$;
This function is taken as the θ_{rec}^{ring} resolution.
In fig.2 (b) the plot of θ_{off} (mrad) (again a gaussian fit to the distributions of fig.1) as a function of β, with superimposed a fit of a function of the form : $f(\beta) = a\ (1\text{-}\beta^2)^{3/2}$ / $(n^2\beta^2\text{-}1)^{1/2}$.
This offset is interpreted as due to the particle energy losses at the RICH entrance and in the radiator gas; in the following analysis, the θ_{rec}^{ring} value is then corrected according to the function given above.
In fig.2 (c) the distribution of $\Delta\theta$ in a range of β close to 1.

It should be stressed that more than 65% of the statistics (in particular the high β particles) stay in the 1^{st} β bin.

In fig.3 $\Delta\theta$ (mrad) is plotted as a function of the particle momentum, in the range $0. \leq p \leq 60.$ GeV/c, in 12 bins of $\Delta p = 5.$ GeV/c.
In fig.4 σ_{θ}^{ring} (mrad), as result of a gaussian fit to the distributions of fig.3, as a function of particle momentum (GeV/c).)

c) Correction for particle m.c.s.

At the RICH entrance the particle undergoes an appreciable multiple coulomb scattering (m.c.s.), function of its momentum.
Requiring that at least one point of the particle trajectory is measured downstream the RICH exit window, part of the effect can be taken into account. Instead of the 'measured' direction of the particle at the RICH entrance window, the direction calculated joining the particle 'measured' position at (or close to) the entrance window to the particle 'measured' position at (or close to) the exit window should be used.
In fig.5 are shown the distributions of $\Delta tg\alpha = tg\alpha_{meas}$-$tg\alpha_{calc}$, in the xz projection plane

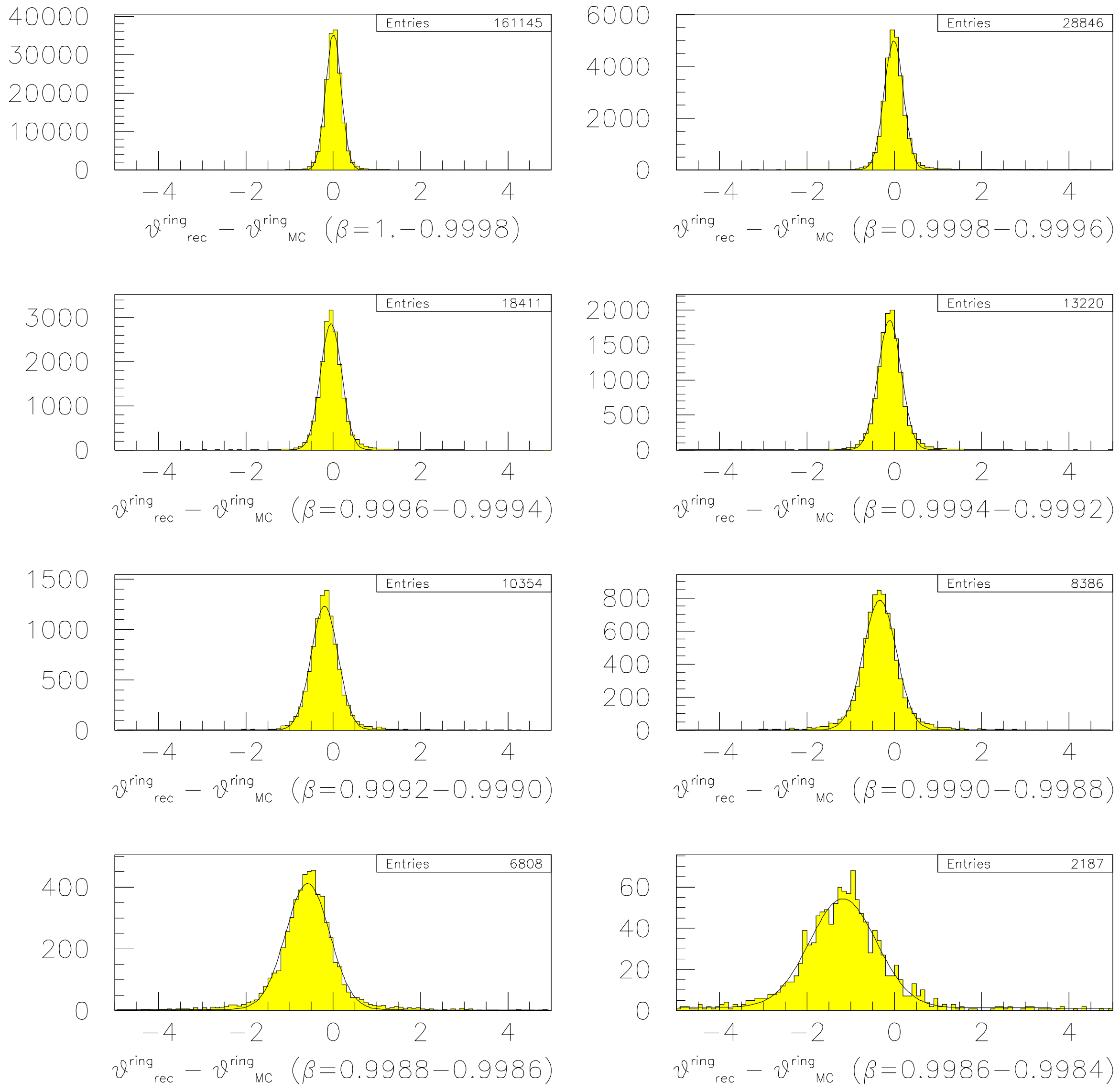

Figure 1: The distribution of θ^{ring}_{rec} - θ^{ring}_{MC} (mrad), in 8 bins of β of the particle.

($\Delta tg\alpha_x$) and in the yz plane ($\Delta tg\alpha_y$), for all momenta.
In fig.6 the lower part of the same distributions as in fig.1, with $\Delta\theta$ computed using the calculated particle direction (i.e. corrected for m.c.s., as in fig.1) (color), together with the the 'uncorrected' ones (white), where $\Delta\theta$ is evaluated from the particle direction at RICH entrance.

d) Monitoring from data.

To have a monitor of the resolution in θ^{ring}_{rec} using the data from the experiment (or MC),
$\Delta\theta$ is defined as in **a)** above, but instead of θ^{ring}_{MC} we compute θ^{ring}_{mass} using the measured particle momentum and the mass, typically, of the π, the K or the p.
The three values of $\Delta\theta$ enter the histograms of figure 7, which are equivalent to those of fig.1; the central peak corresponds to the correct mass hypotesis and it remains enough separated, even in the β bin close to 1., to allow an evaluation of σ^{ring}_{θ}.

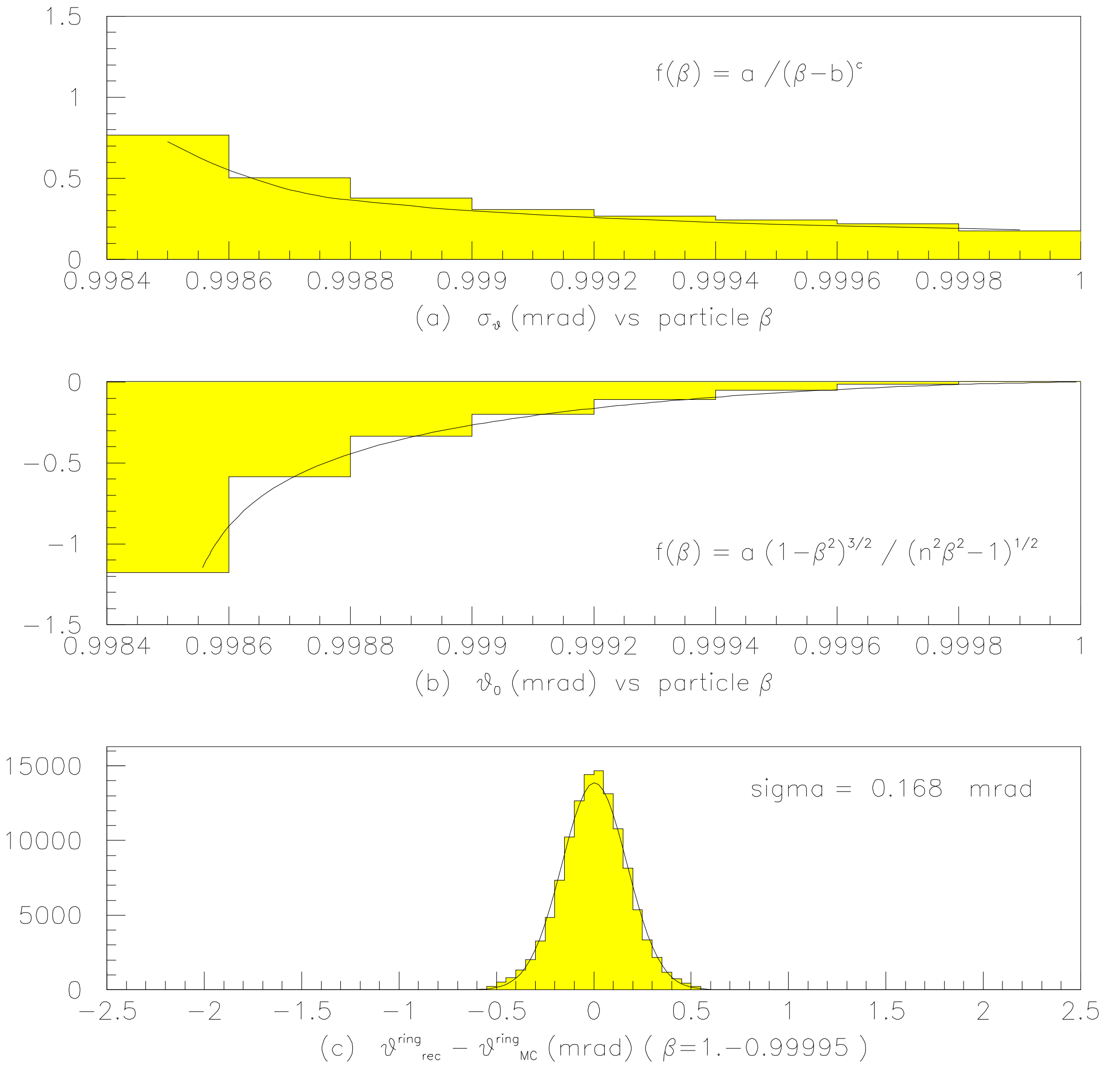

Figure 2: (a) σ_θ^{ring} (mrad), from a gaussian fit to the distributions of fig.1, as a function of β; the curve is a fit with a function of the form indicated, with a =0.00518, b =0.99837 and c =0.55. (b) θ_{off} (mrad), again from a gaussian fit to the distributions of fig.1, as a function of β; the fit is with a function of the form indicated, with a = -96.5. (c) The distribution of $\Delta\theta$ (mrad) in the β range close to 1, to show the best resolution value.

In fig.8 (a) σ_θ^{ring} (mrad) (again a gaussian fit to the distributions of fig.7) is shown as a function of β and in fig.8 (b) θ_{off} (mrad) as a function of β; note the good agreement with the MC values of fig.2, apart the last, less significant, β bin.

4 RECONSTRUCTION EFFICIENCY

a) Definition.

The following definition of efficiency is used in the pattern recognition studies :

For each particle 'accepted' (i.e. worth to be processed), the *ring* is reconstructed.

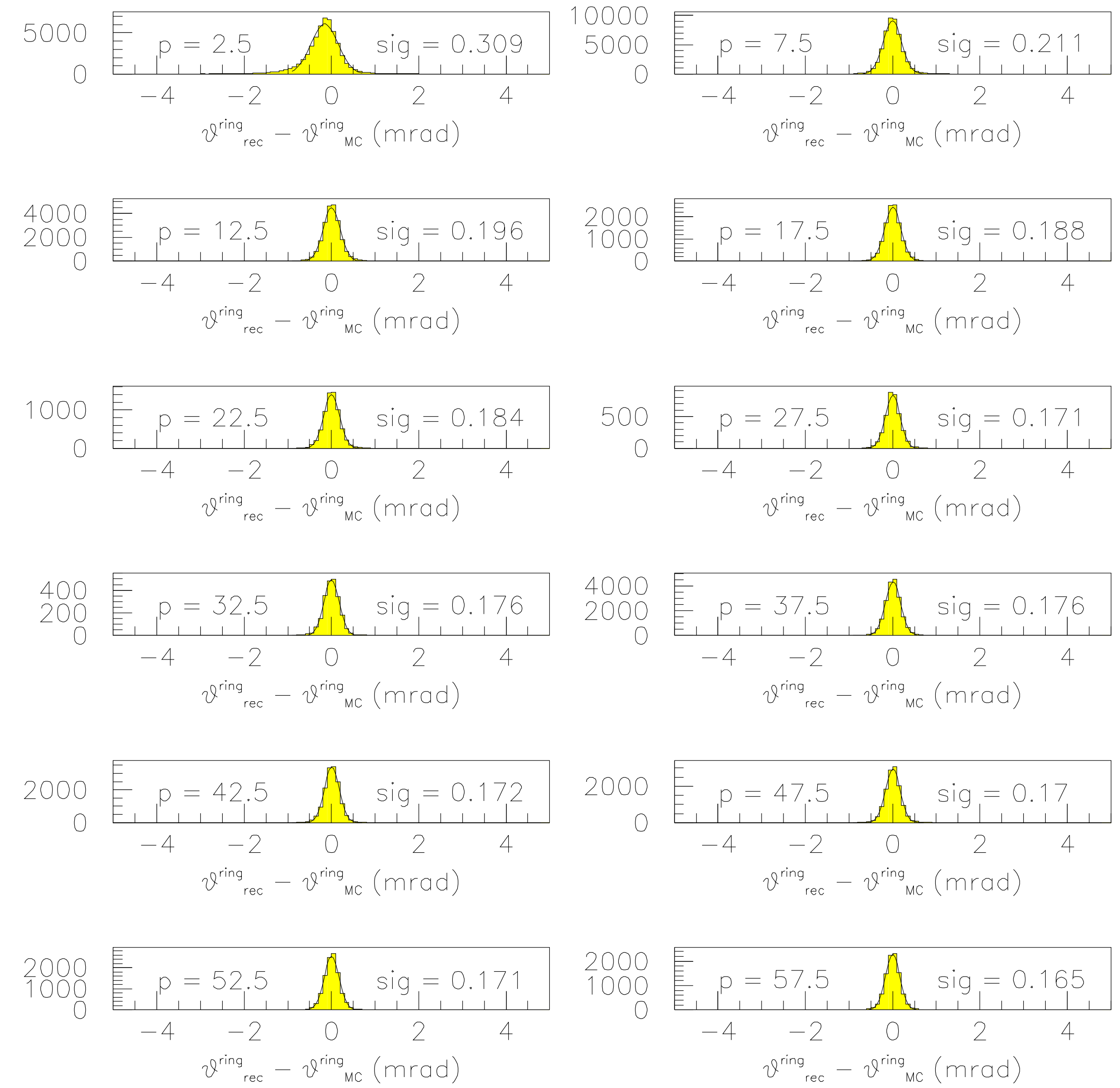

Figure 3: The distribution of θ^{ring}_{rec} - θ^{ring}_{MC} (mrad), in 12 bins of the momentum of the particle (GeV/c), as shown.

Note that a characteristic feature of this method is that for each particle a '*ring*' is found in any case, down to only one photon, signal or background.
To determine wheather the *ring* corresponds to the Cerenkov emission, the reconstructed angle (θ^{ring}_{rec}) is compared to that (θ^{ring}_{MC}) computed from the particle momentum and mass, as from the MC generation data; the *ring* is then 'reconstructed' if the difference $\Delta\theta$ is less than some tolerance, typically $3 \times \sigma^{ring}_{\theta}$.
σ^{ring}_{θ} (the (inverse) θ_C resolution) is a function of the particle β and can be evaluated from the distribution of $\Delta\theta$, as shown in the previous section.

Note that this definition of the reconstruction efficiency is based on a simplified particle identification.

b) Accepted particles.

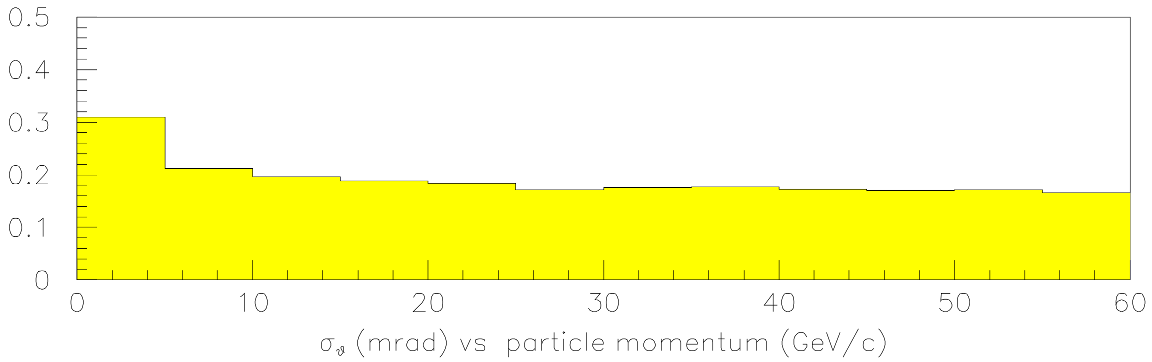

Figure 4: σ_θ^{ring} (mrad) (from a gaussian fit to the distributions of fig.3) as a function of the particle momentum (GeV/c);

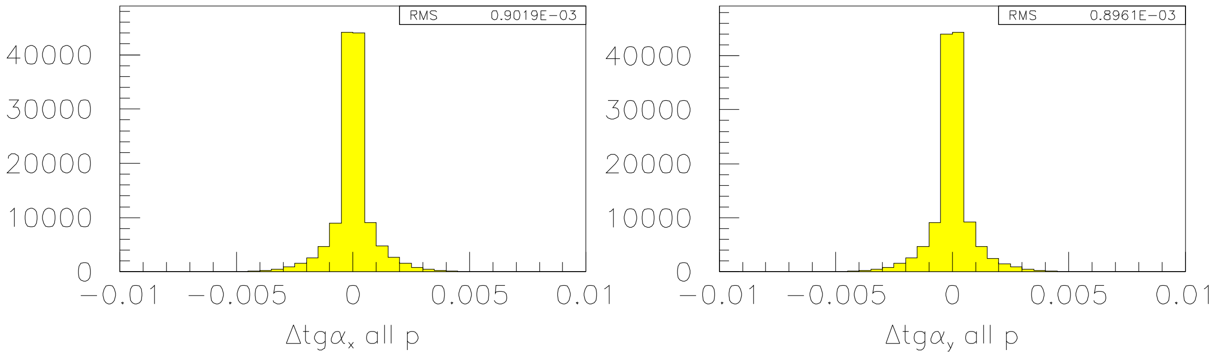

Figure 5: $\Delta tg\alpha = tg\alpha_{meas}$-$tg\alpha_{calc}$ (see text), in the xz projection plane ($\Delta tg\alpha_x$) and in the yz plane ($\Delta tg\alpha_y$), for all momenta.

In the MonteCarlo framework, the characteristics of all the particles of each event are known; the particles can then be selected to study the RICH response.
As far as the present study is concerned, the aim is to determine the efficiency in conditions as close as possible to the experiment.
To do that, a minimal cleaning of the particle sample is done, not processing for ring search :
1 - the particles which interact before reaching the RICH exit window (uses MC flags);
2 - the particles which are outside the cuts described in section **c)** below (see fig.12 (b)), i.e. are undergoing a too much large m.c.s. (or interacting).

c) Efficiency with MC events.

The reconstruction efficiency, as defined in point a) above, has been evaluated as a function of β of the particle, of its momentum and of the number of photons found in the reconstructed *ring*.

In fig.9 (a) the distribution of the particles accepted (white) and with a ring reconstructed (color) as a function of β; note how most of the statistics is concentrated in the β bin close to 1., mainly because the scattered μ^s are included in the particle sample.
In fig.9 (b) the efficiency (the ratio of the two distributions shown in (a)) as a function of β, together with the average value; the decrease of the efficiency with β is quite evident,

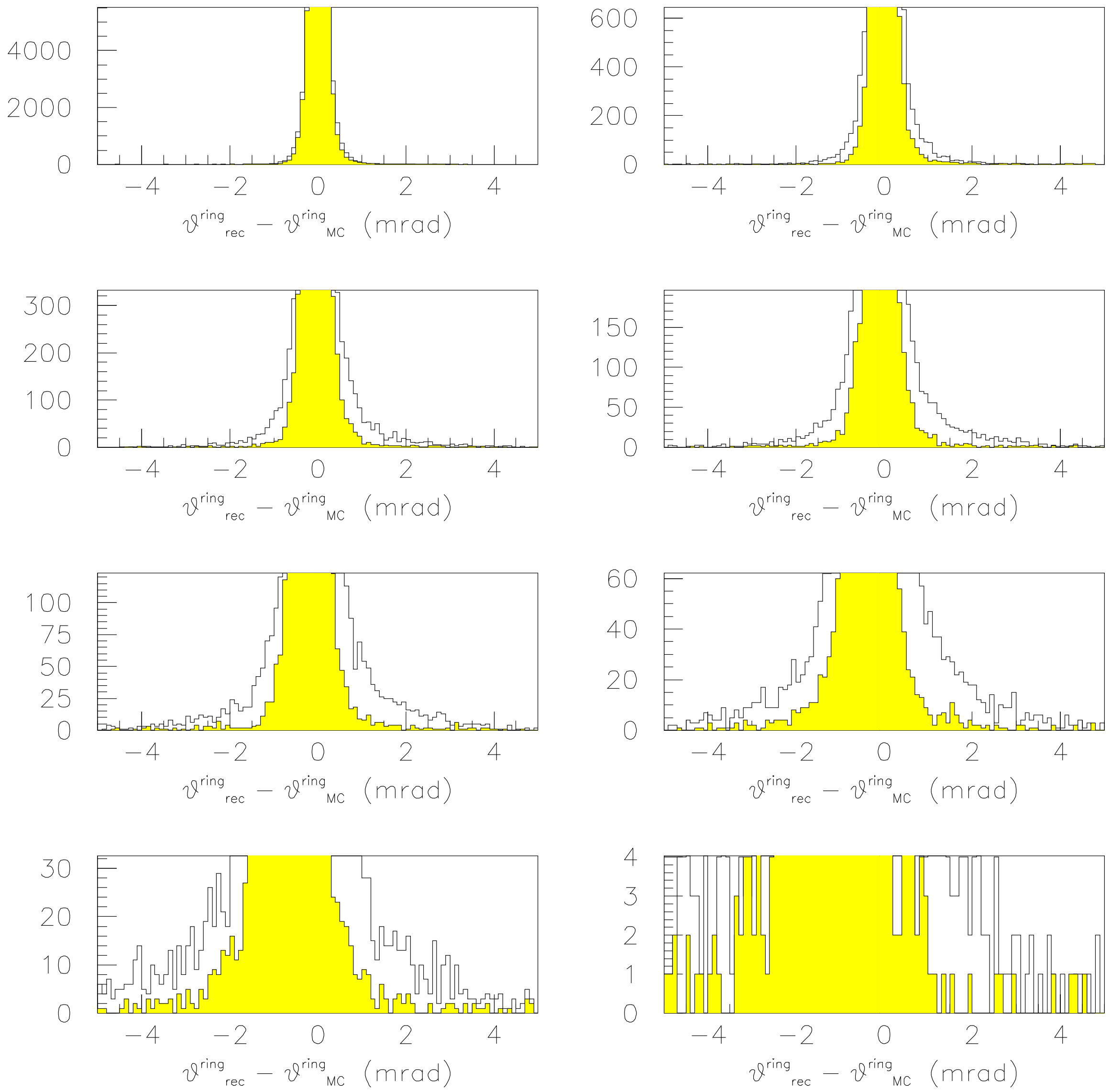

Figure 6: The lower part of the distributions of fig.1, with $\Delta\theta$ computed using the calculated particle direction (i.e. corrected for m.c.s.) (color), together with the the 'uncorrected' ones (white), where $\Delta\theta$ is evaluated from the particle 'measured' direction.

essentially because the number of Cerenkov photons emitted decreases with β.

As can be noted from fig.1 and fig.6 the background under the signal peak is rather small for all the β bins; a cut at $4 \times \sigma_\theta^{ring}$ for the efficiency definition (instead of $3\ \times$), is still acceptable and it results in an increase of the average efficiency from 0.96 to 0.97, mainly contributed from low β bins.

In fig.10 (a) the momentum spectra of the processed particles are shown; the particle types are essentially pions, kaons, protons and muons (scattered and from decay); in fig.10 (b) the reconstruction efficiency as a function of the particle momentum, with superimposed the average efficiency.

In fig.11 (a) The distribution of accepted particles and reconstructed *rings* (color)

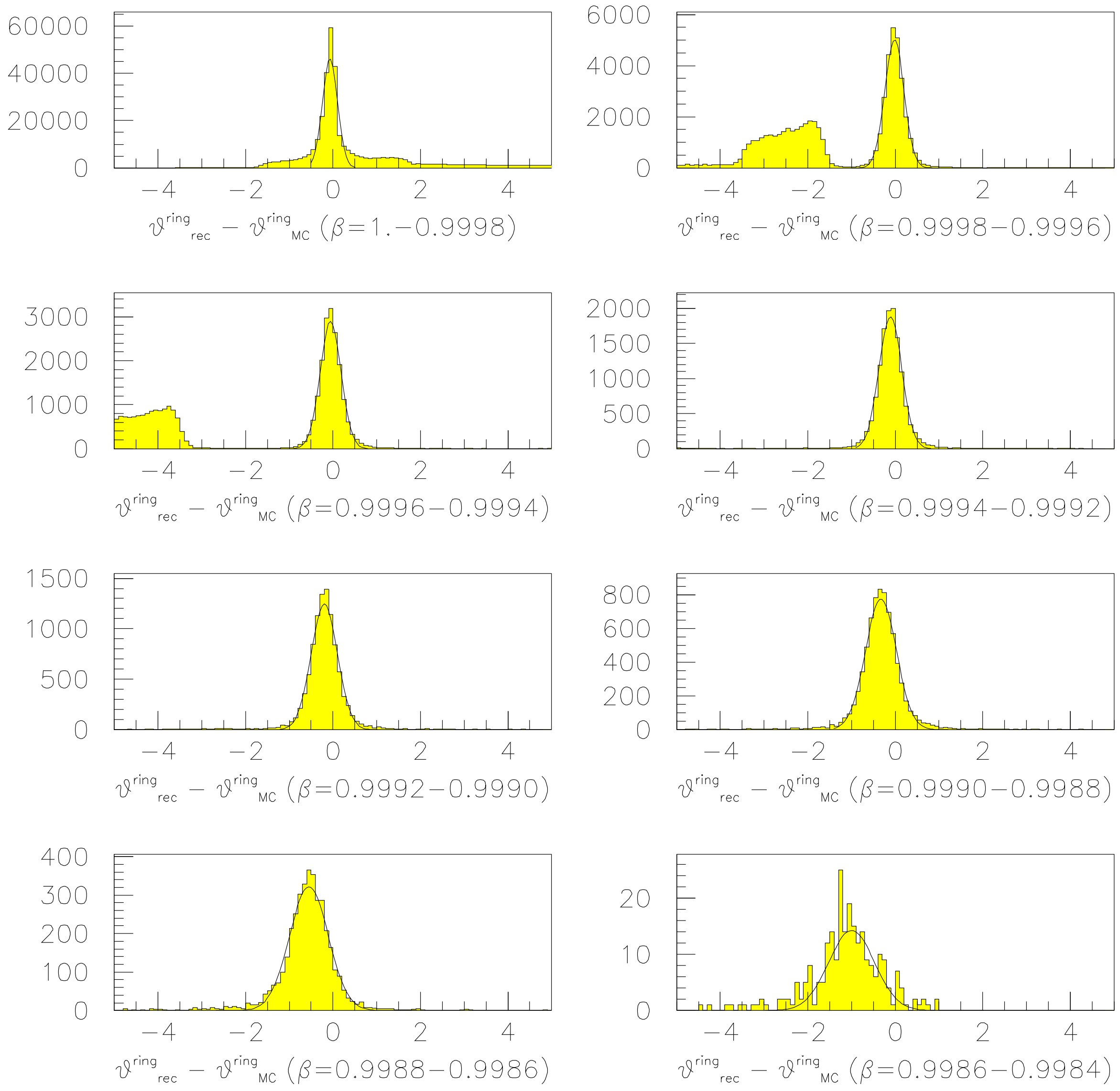

Figure 7: The distribution of θ^{ring}_{rec} - θ^{ring}_{mass} (mrad), in 8 bins of β of the particle.

as a function of the number of photons found on each *ring* in the reconstruction; note how the bins are well populated down to one photon. In fig.11 (b) the reconstruction efficiency as a function of the number of photons per *ring*.

It is clear that a threshold on a minimum number of photons per *ring* could be foreseen to deal with a more convincing sample of *rings*; nevertheless, at least in the present situation of the simulation (mainly as regards the background level) the method shows its power and gives good reconstruction even for a number of photons per *ring* as low as 1.
Accepting *rings* with, say, more than 4 photons reconstructed on them, the average efficiency grows of about 1%, as expected from fig.11 (a) assuming as denominator the corresponding number of particles. In the real life the accepted particle sample will be fixed by the experimental conditions and a cut in the minimum number of photons will result in any case in non-reconstructed *rings* with a consequent loss in efficiency.

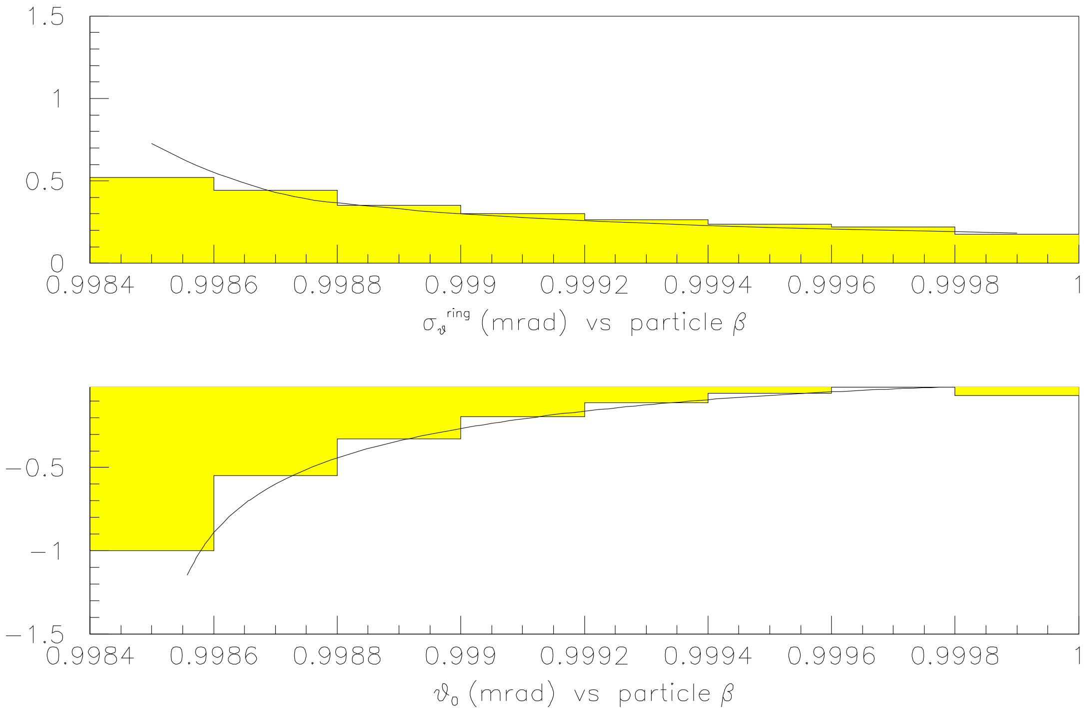

Figure 8: (a) σ_θ^{ring} (mrad), from a gaussian fit to the distributions of fig.7, as a function of β; the curve is the same function as in fig.2 (a), (b) θ_{off} (mrad), again from a gaussian fit to the distributions of fig.7, as a function of β; same function as in fig.2 (b).

In fig.12 (a) The distribution of the incoming particle types at the RICH entrance window, according to GEANT coding (i.e.: 1 = incoming beam particle (μ^+), 2,3 = e^+, e^-, 5,6 = μ^+, μ^-, 8 to 10 = π^+, π^-, π^0, 11 to 13 = K^+, K^-, K^0, 14,15 = $p, \bar{p}$, ...); the colored areas correspond to particles rejected on the basis of the direction filter at the exit window and then not processed for *ring* reconstruction.
The plot in fig.12 (b) shows the distribution of Δr (mm) the radial distance between the point in which the particle crosses the RICH exit window and the projection on the exit window of the particle trajectory at the entrance window, as a function of the particle momentum (GeV/c); the line is the boundary outside which particles are rejected, essentially to avoid particle interactions at the RICH entrance or inside the radiator.

In fig.13 (a) there is the distribution of the number of the reconstructed photons per *ring* as a function of the particle β; the Cerenkov emission threshold for the radiator used (C_4F_{10}) is at β=0.99847 (vertical line); the line is a fit of the form $n(\beta) = N_0\ sin^2\theta = N_0\ (1 - 1/(n_r\ \beta)^2)$, where n_r is the radiator refraction index ($n_r = 1.00153$). There is still some discrepancy, but the value of N_0 obtained is in rather good agreement with the MC generation figure ($N_0 = 30$, i.e. fixed number of generated photons).

In fig.13 (b) is shown the value (mrad) of the reconstructed Cerenkov emission angle θ_{rec}^{ring} as a function of β (as reconstructed); the line superimposed is $\theta_C(\beta) \simeq \sqrt{2\ (1 - 1/(n_r\ \beta))}$ and the agreement is rather good.

In fig.13 (c) is reported the product $cos(\theta_{rec}^{ring})\ n_r\ \beta$, as a function of β, to be compared with the constant value of 1; there is still some disagreement close to the threshold.

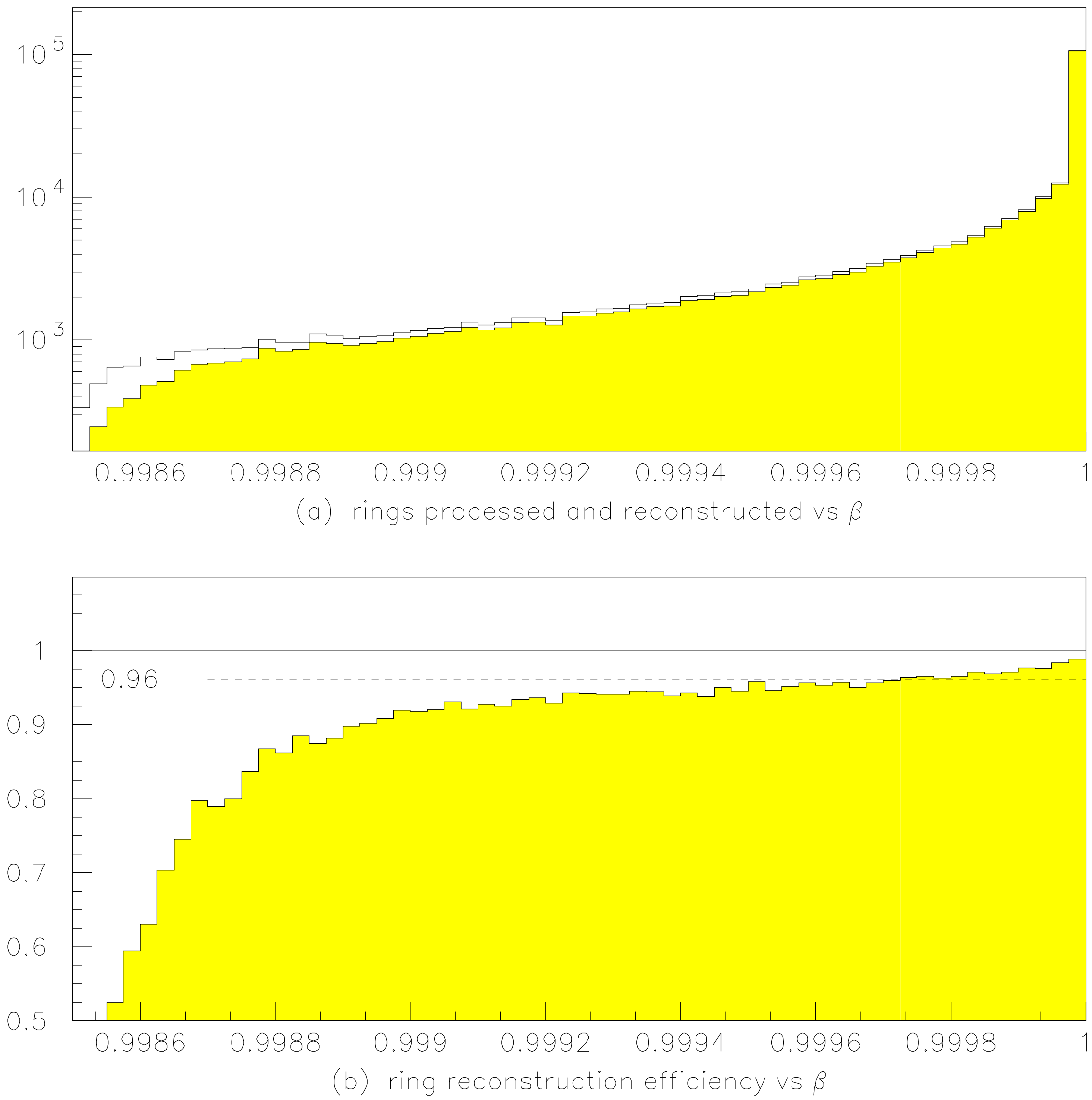

Figure 9: (a) Particles processed and *rings* reconstructed (color) as a function of particle β. (b) The reconstruction efficiency (ratio of reconstructed over accepted) as a function of β; the broken line is the average efficiency.

Note that in the plots of fig.13 the value of θ_{rec}^{ring} has already been corrected for the offset $\theta_{off}(\beta)$ due to the energy losses.

d) Monitoring of the efficiency from data.

The reconstruction efficiency can usefully be monitored from data using a modified definition of efficiency : as for resolution monitoring, instead of θ_{MC}^{ring} we use θ_{mass}^{ring} (as defined in section **3 - d** above) to compute $\Delta\theta$; the *ring* is assumed as reconstructed if at least one of the $\Delta\theta'^s$, corresponding to the different mass hypotheses, is within the 3 $\times$ (or 4 $\times$) σ_θ^{ring} tolerance.
In fig.14 (a) the distribution of the particles processed (white) and with a ring accepted as reconstructed (color) as a function of β is shown;

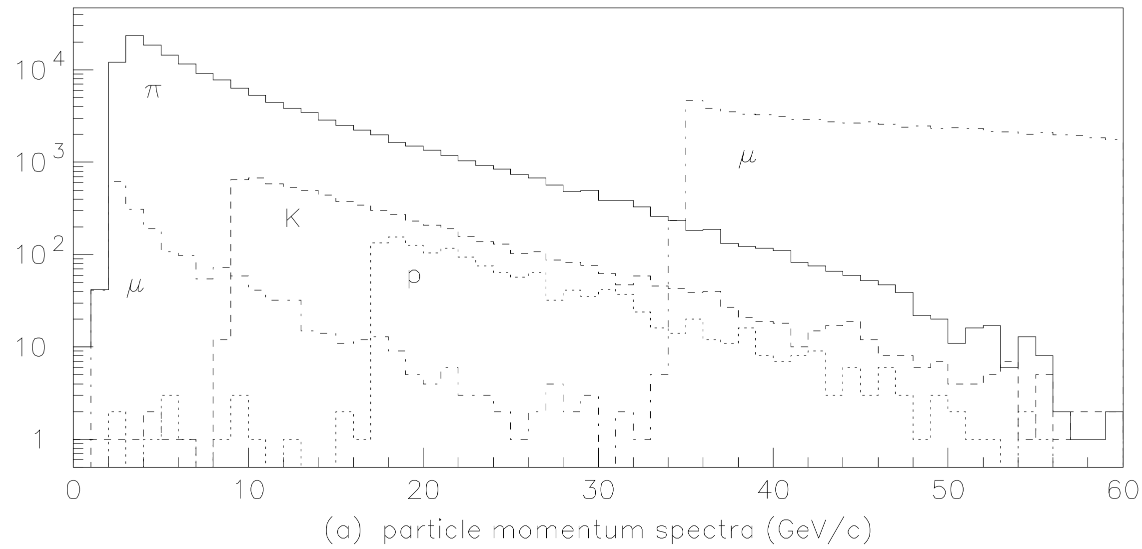

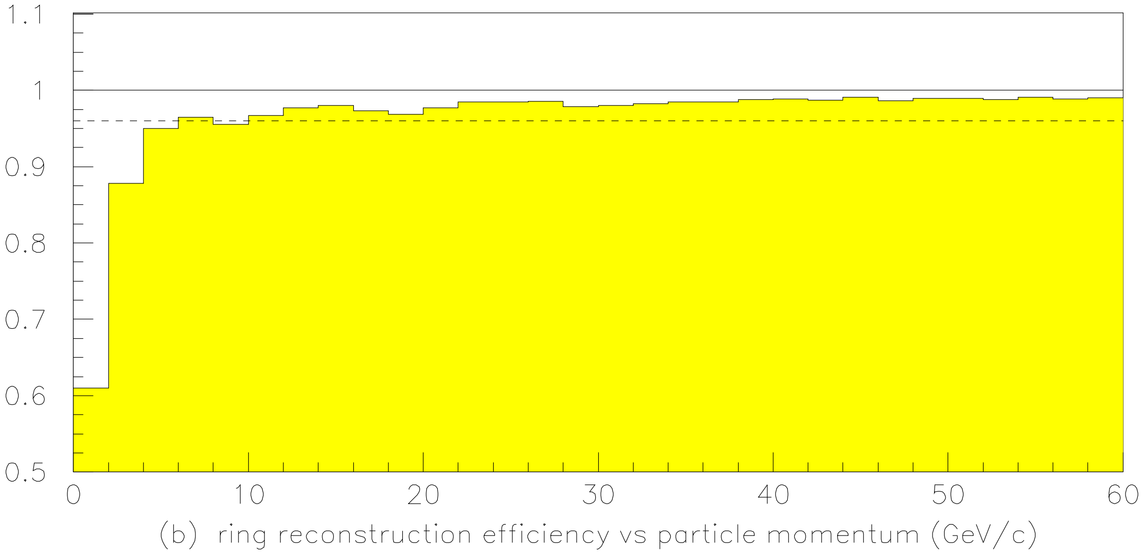

Figure 10: (a) Processed particle spectra (particle types as indicated). (b) The reconstruction efficiency as a function of particle momentum; the broken line is the average efficiency.

In fig.14 (b) the efficiency (the ratio of the two distributions shown in (a)) as a function of β, together with the average value; to be compared with the distributions of fig.9 (a) and (b).

In fig.15 (a) the overall momentum spectrum of the processed particles is shown; in fig.15 (b) the monitored reconstruction efficiency as a function of the particle momentum together with the average efficiency (broken line). Compare with the distributions of fig.10 (a) and (b).

In fig.16 the distribution of the multiplicity of the clusters found on *ring* is shown.

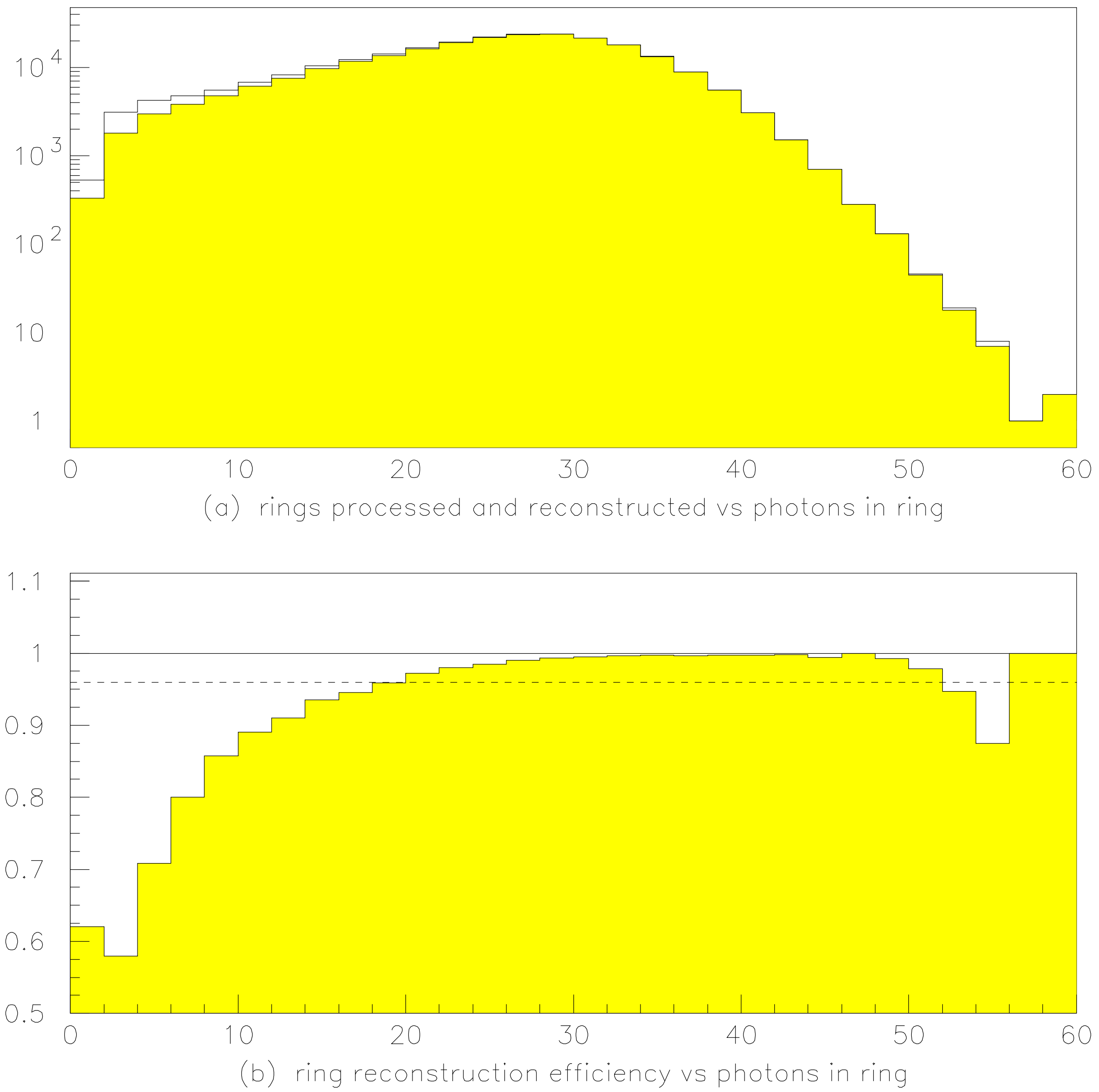

Figure 11: (a) The distribution of accepted particles and reconstructed *rings* (color) as a function of the number of photons found on each *ring* in the reconstruction. (b) the reconstruction efficiency.

5 PARTICLE IDENTIFICATION

a) χ^2 calculation

In the present preliminary approach, the mass assignment to the particle for which a *ring* has been reconstructed is done on a χ^2 basis.
The masses of μ, π, K or p are taken into account. For a given mass hypothesis and from the (measured) particle momentum, β is calculated and checked for being over the Cerenkov emission threshold; in this case, θ_{calc}^{ring} is calculated from β and the radiator refraction index.
A χ^2_{mass} is then computed summing over all the photons in the *ring* the terms $(\theta_{rec}^{photon} - \theta_{calc}^{ring})^2/(\sigma_\theta^{photon})^2$; as a figure of merit to choose among the different hypothesis, the value of the χ^2_{mass}, divided by the number of photons in the *ring*, (or the corresponding prob-

ability) is taken and the least χ^2_{mass} selected.
σ_θ^{photon} is the standard deviation of the distribution of θ_{rec}^{photon}, the angle of each photon reconstrucetd in the *ring*, around θ_{rec}^{ring} and it is a function of particle β and other geometrical quantities as dicussed below. The photons entering the sum of χ^2_{mass} (i.e. belonging to the *ring*), can be selected on the basis of their distance to the reconstructed *ring* (θ_{rec}^{ring}) in terms of (typically $3\times$) σ_θ^{photon}.
A χ^2_{ring} is also computed summing over all the photons in the *ring* the terms $(\theta_{rec}^{photon} - \theta_{rec}^{ring})^2/(\sigma_\theta^{photon})^2$ and dividing by the number of degrees of freedom.

In fig.17 (a) the distribution of the least χ^2_{mass} is shown; the broken line is the expected average value, to be compared with the actual value, in the upper right corner, due mainly to the tail of the distribution. The fig.17 (b) shows the same distribution as in (a) together with the χ^2_{ring} distribution (color), in quite good agreement.

b) Resolution in the photon angle.

The knowledge of σ_θ^{photon} is needed not only in χ^2 calculations but mainly in the *ring* recognition procedure.
σ_θ^{photon} has been evaluated independently using essentially no cuts in the *ring* reconstruction definition; in fig.18 the distribution of $\theta_{rec}^{photon} - \theta_{rec}^{ring}$ is shown for all the photons processed in the *ring* recognition for each particle; θ_{rec}^{photon} is the reconstructed angle each emitted photon makes with the particle trajectory direction. The distribution has been fitted with a gaussian plus a linear background to extract the resolution in θ_{rec}^{photon}.
The dependence of σ_θ^{photon} on various quantities has been investigated; the most relevant ones are the particle β, discussed in the following, and the photon azimuthal angle around the particle direction, not discussed in the present report; further dependences, like on the 'reflected particle'-detector angle, have been found negligeable.
The fig.19 shows the same distribution as in fig.18 in bins of β, from threshold to 1. and fig.20 shows a fit to $\sigma_\theta^{photon}(\beta) = a + b(1-\beta^2)$, with a = 0.8 and b = 62., which has been used in the analysis; the dependence on β results rather small.

c) Particle identification.

In fig.21 the particle mass assignment is reported; the columns represent the particle types as indicated, known from MC input; the rows, the particle types as identified with the procedure of section **a)** above. It is evident, as expected, that the RICH is not able to separate $\mu's$ from higher masses and that an independent μ identification is necessary. Fig.22 shows the same results for π, K and p only, in momentum bins of 5.GeV/c ranging from 0. to 60.GeV/c. The wrong assignments, in particular between $\pi's$ and $K's$, can be evaluated in percentage.

6 ELECTRONIC NOISE TESTS

It is planned to use a hardware threshold in RICH data acquisition and a software one in data analysis. In the present simulation, one threshold is used, set at 3 σ from the average pedestal value. Moreover, in the simulation, an electronic noise is random distributed over the photon chamber pads with a gaussian distribution in pad pulse height.

The setting of the threshold determines the fraction of pads activated due to electronic background.
Some tests in a quite preliminary form have been carried out to have an idea of the dependence of the RICH response on the background level. The threshold has been lowered to 2.5 and 2. σ respectively.
Results are summarized in fig.23; in (a) is shown the average cluster size and in (b) the average cluster size for clusters on the reconstructed *rings*, for 3 σ threshold (white), 2.5 σ (grey) and 2 σ (dark grey). In (c), (d) and (e) the active pad distribution for the three values of the threshold; the signal, contributing for less than 80 pads in average, is also counted; this results in a about 0.25%, 0.75% and 2.5% respectively of pads activated. In fig.23 (f) the reconstruction efficiency as a function of the particle momentum for the three threshold values (same color code as in (a) and (b)); the loss in efficiency for higher background is quite appreciable.
The fig.24 is intended to give an immediate appreciation of the background level for the three threshold value, 3 σ (a), 2.5 σ (b) and 2 σ (c).
It is clear that in the experiment a threshold of 3 σ or higher should be used.

7 EVENT DISPLAY

To study and check the reconstruction procedure, an event display has been build, allowing to better understand many less evident situations.
In fig.25 a general view of (the relevant part of) the eight photon chambers (four upper and four lower; the dimensions are in mm) is presented; four incoming particles are simulated, but only three have been accepted for *ring* reconstruction processing (see section ...) and the *rings* successfully reconstructed; the photons of the non-processed particle are visible in the upper right corner of the picture.
In fig.26 one of the reconstructed particles is shown in detail in an enlarged scale; the black squares, which have the dimensions (8×8 mm^2) of a detector pad, represent the clusters as found in the clustering procedure, belonging to the *ring* presented; the grey squares are the active pads as given by the detector read-out, background included. In both pictures the circles superimposed are a simple fit to guide the eye; the continuous line is the reconstructed value, the broken one, the predicted; the crosses in the centre are the virtual impact points on the detector surface of the 'reflected' particles.
In the upper part of the plot the histogram superimposed shows the 'peak' in the θ_{rec}^{photon} distribution for the particle considered on which the recognition procedure is based; the thick line is the average θ_{rec}^{photon} value ($= \theta_{rec}^{ring}$), the broken line the θ_{MC}^{ring} predicted by MC and the two thin ones the $2 \times 3 \times \sigma_\theta$ window.

In fig.27 is shown an exemple of a *ring* with only two photons on it; in this plot the reconstructed θ_{rec}^{ring} has not yet been corrected for the (rather low β) particle energy losses; this explain the difference between the reconstructed and MC predicted *ring* radius (smaller than the 3 $\times \sigma_\theta$ tolerance).

In fig.28 and 29 are shown two exemples of *rings* wrongly reconstructed for two of the many different reasons which determine the residual inefficiecy of the reconstruction. In fig.28 a rather low β particle with possibly only one photon on its *ring* has been confused with photons belonging to other particles or to background; in fig.29 two particles are giving origin to almost concentric *rings*; this is a typical situation of confusion and some improvements to the procedure are under study.

8 CONCLUSIONS

The response of the procedure is rather satisfactory, at least in the limits of the simulation used.
It seems to be an acceptable basis for a reconstruction program for COMPASS RICH 1.

The corresponding computer code is available in a FORTRAN as well as in a C^{++} version, with exactly equivalent results, apart from the execution time, which results a factor of about 1.7 larger for C^{++}.

The next step is its the integration in the COMPASS CORAL reconstruction program, which is planned to start beginning of March 2000.

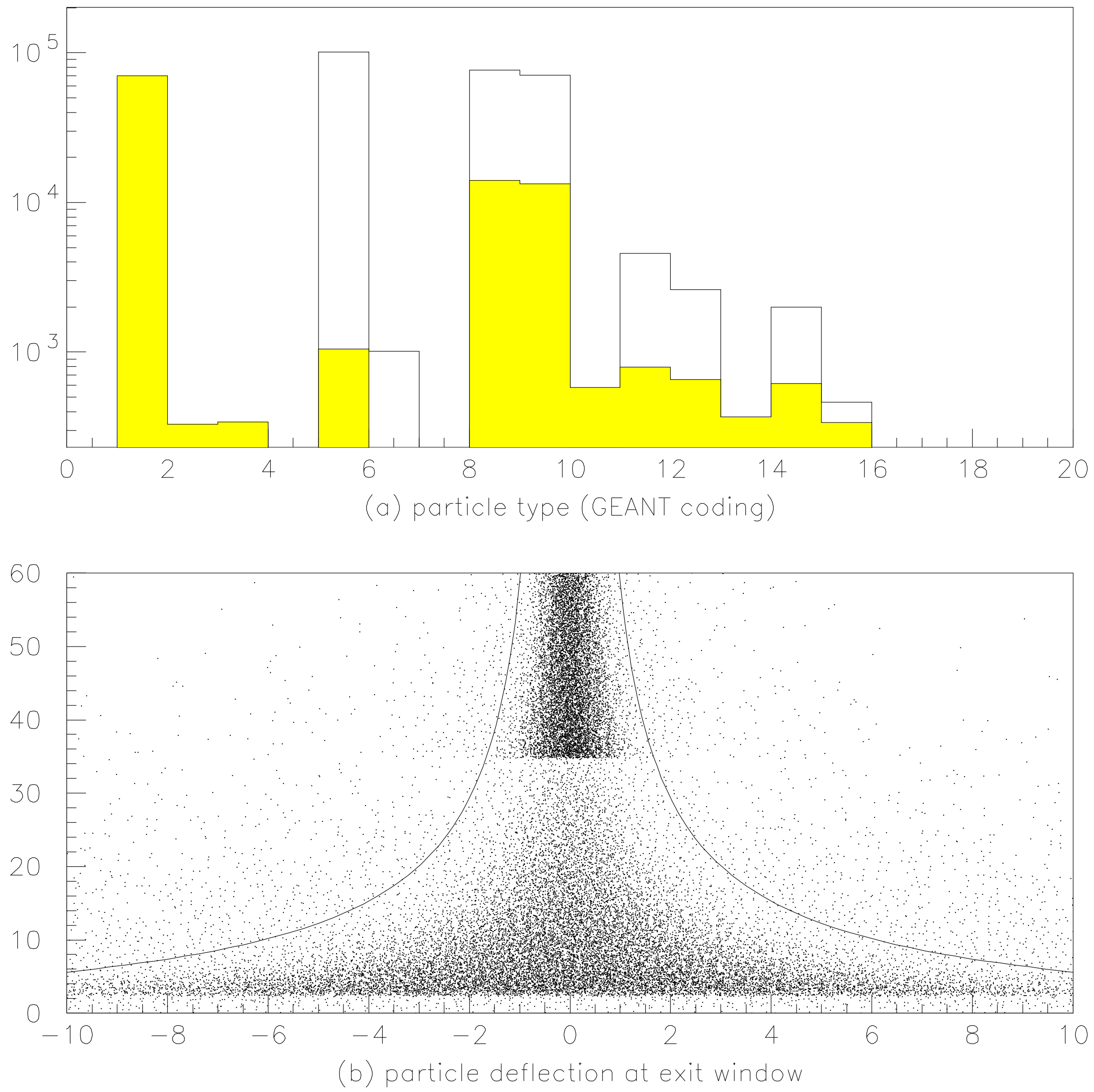

Figure 12: (a) The distribution of the incoming particle types at the RICH entrance window, according to GEANT coding (see text); the colored area represents the particles outside the cut shown in (b). (b) The plot of Δr (mm), the radial distance on the RICH exit window between the particle crossing point and the projection of the particle trajectory at the entrance window, as a function of the particle momentum (GeV/c); the line is the cut used to reject the interacting particles.

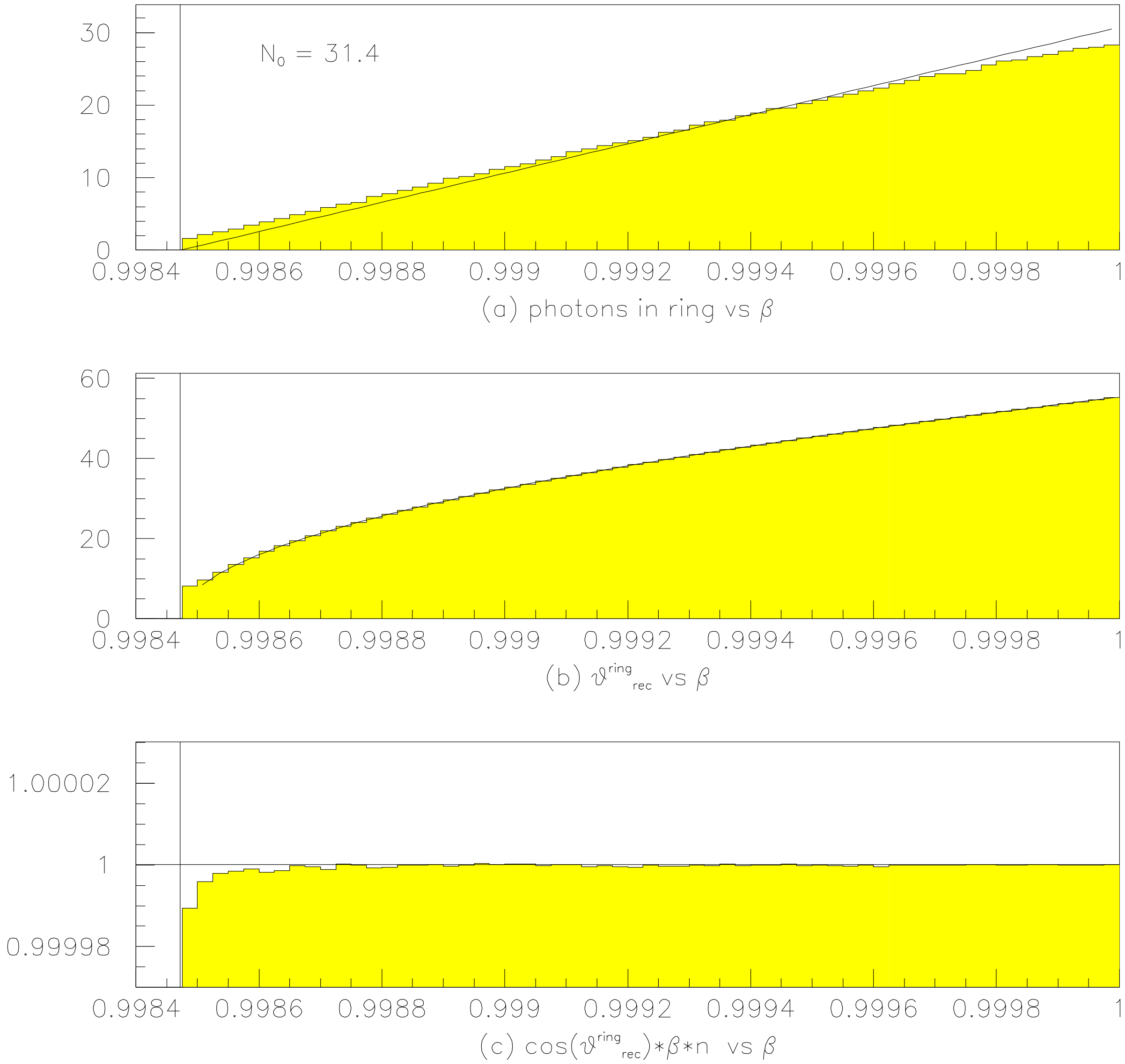

Figure 13: (a) the distribution of the number of the reconstructed photons per *ring* as a function of the particle β; the vertical line is the Cerenkov emission threshold for the radiator used; the line is a fit of the form $n(\beta) = N_0\ sin^2\theta$. (b) The reconstructed Cerenkov emission angle θ_{rec}^{ring} as a function of β (as reconstructed); the line superimposed is $\theta_C(\beta) \simeq \sqrt{2\ (1 - 1/(n_r\ \beta))}$. (c) The product $cos(\theta_{rec}^{ring})\ n_r\ \beta$, as a function of β, to be compared with the constant value of 1.

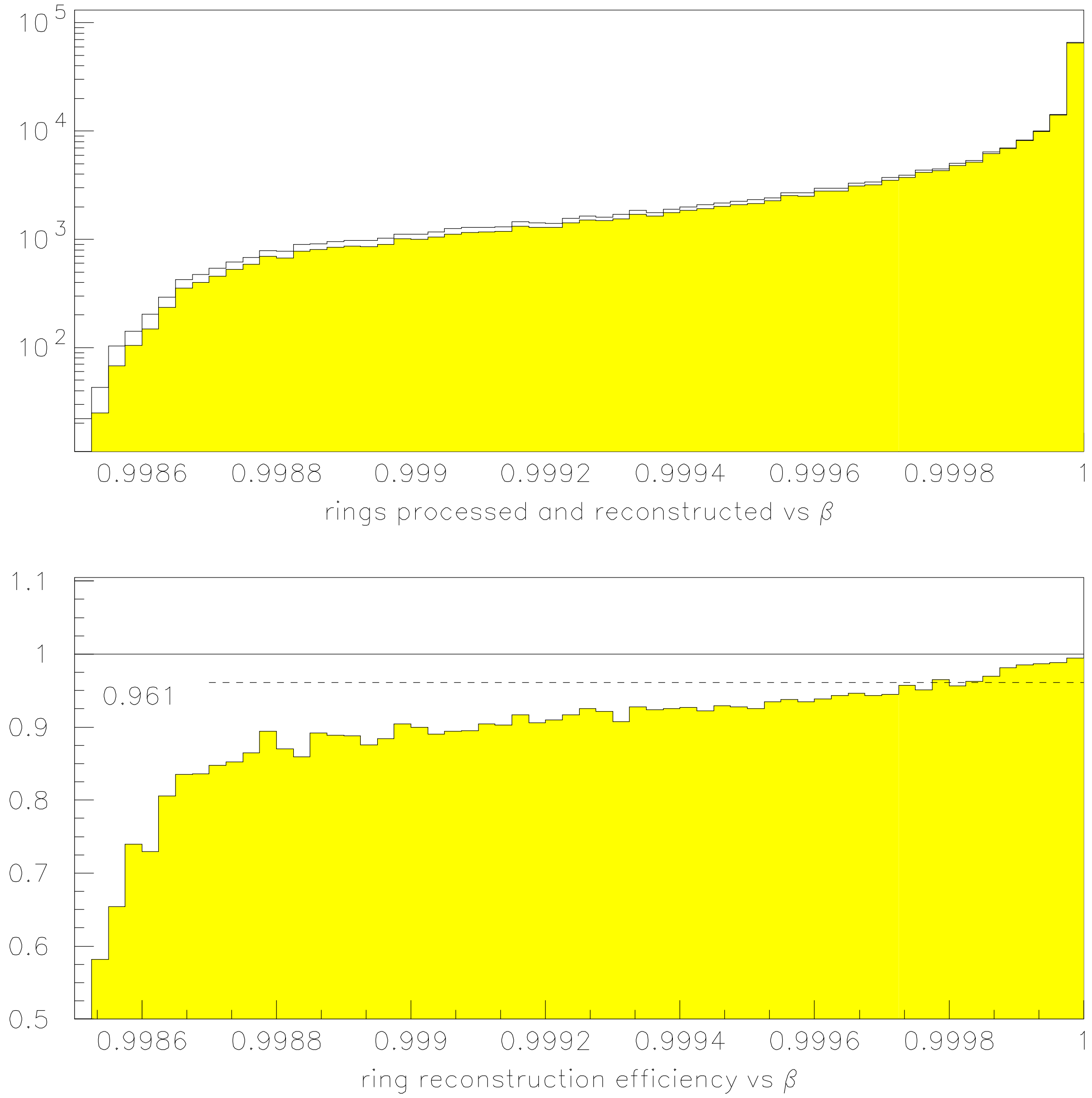

Figure 14: (a) Particles processed and *rings* accepted as reconstructed (color) as a function of particle β. (b) The monitored reconstruction efficiency as a function of β; the broken line is the average value. Compare with the distributions of fig.9

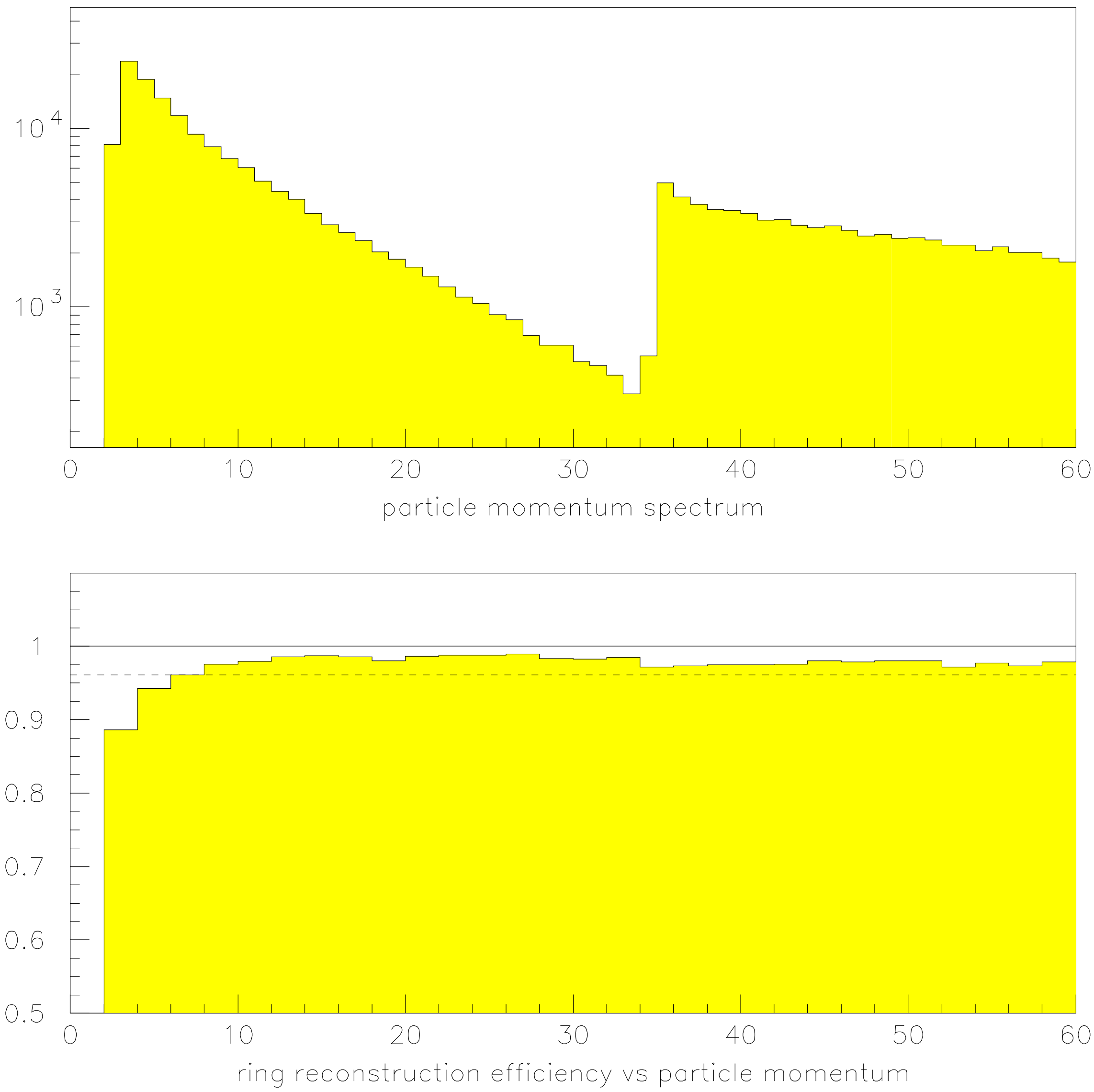

Figure 15: (a) Momentum distribution of the processed particles. (b) The monitored reconstruction efficiency as a function of particle momentum; the broken line is the average efficiency. Compare with the distributions of fig.10

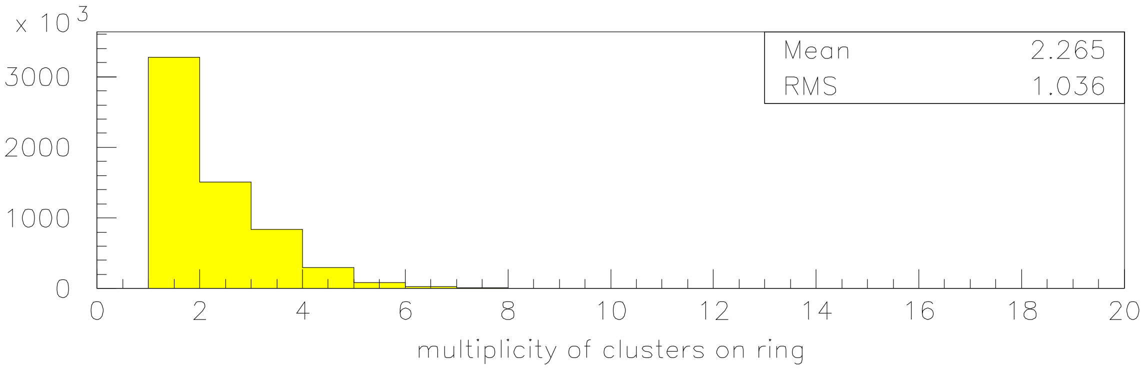

Figure 16: The distribution of the multiplicity of the clusters found on *ring*.

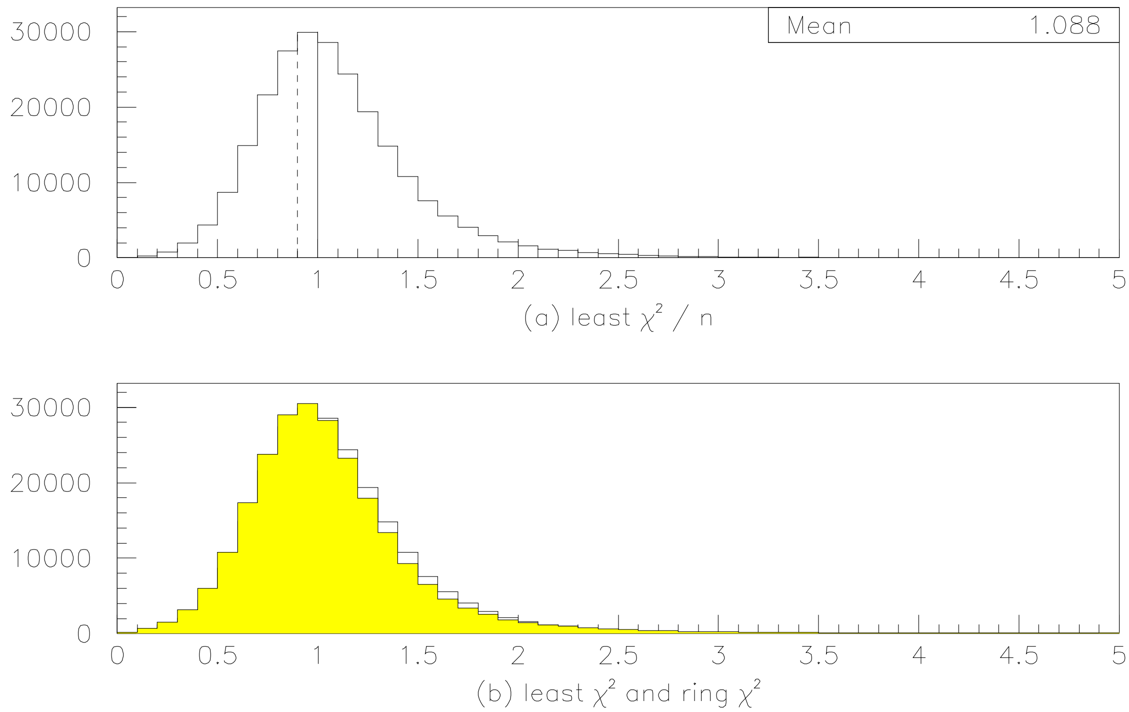

Figure 17: (a) The distribution of the least χ^2_{mass} among the different mass hypotheses. (b) The distribution in (a) together with the distribution of the χ^2_{ring}, for comparison.

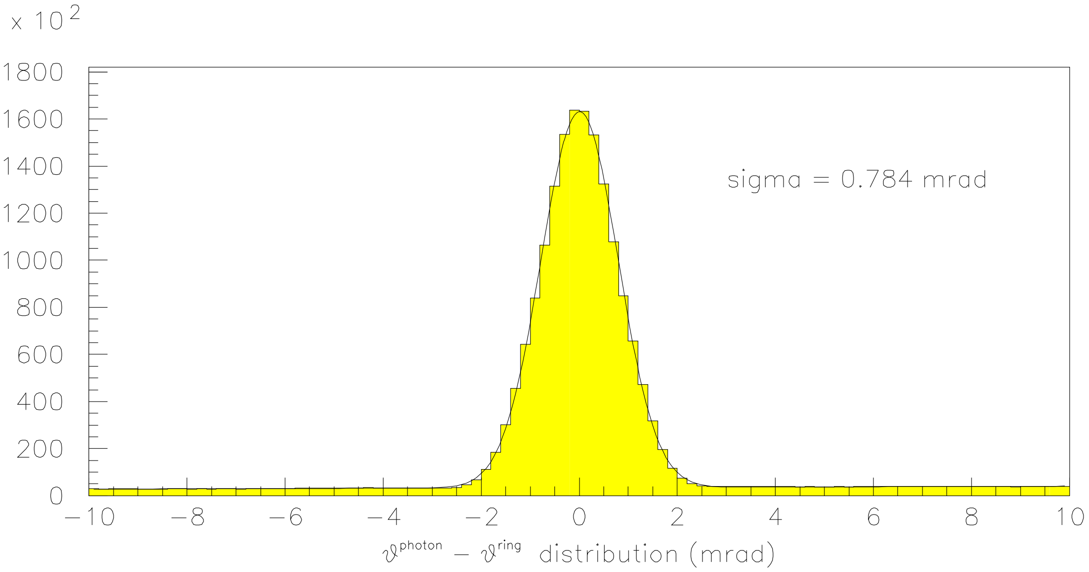

Figure 18: The distribution of $\theta^{photon}_{rec} - \theta^{ring}_{rec}$ for all the photons processed in the *ring* recognition for each particle. The fit is to gaussian plus a linear background to extract the resolution in θ^{photon}_{rec}.

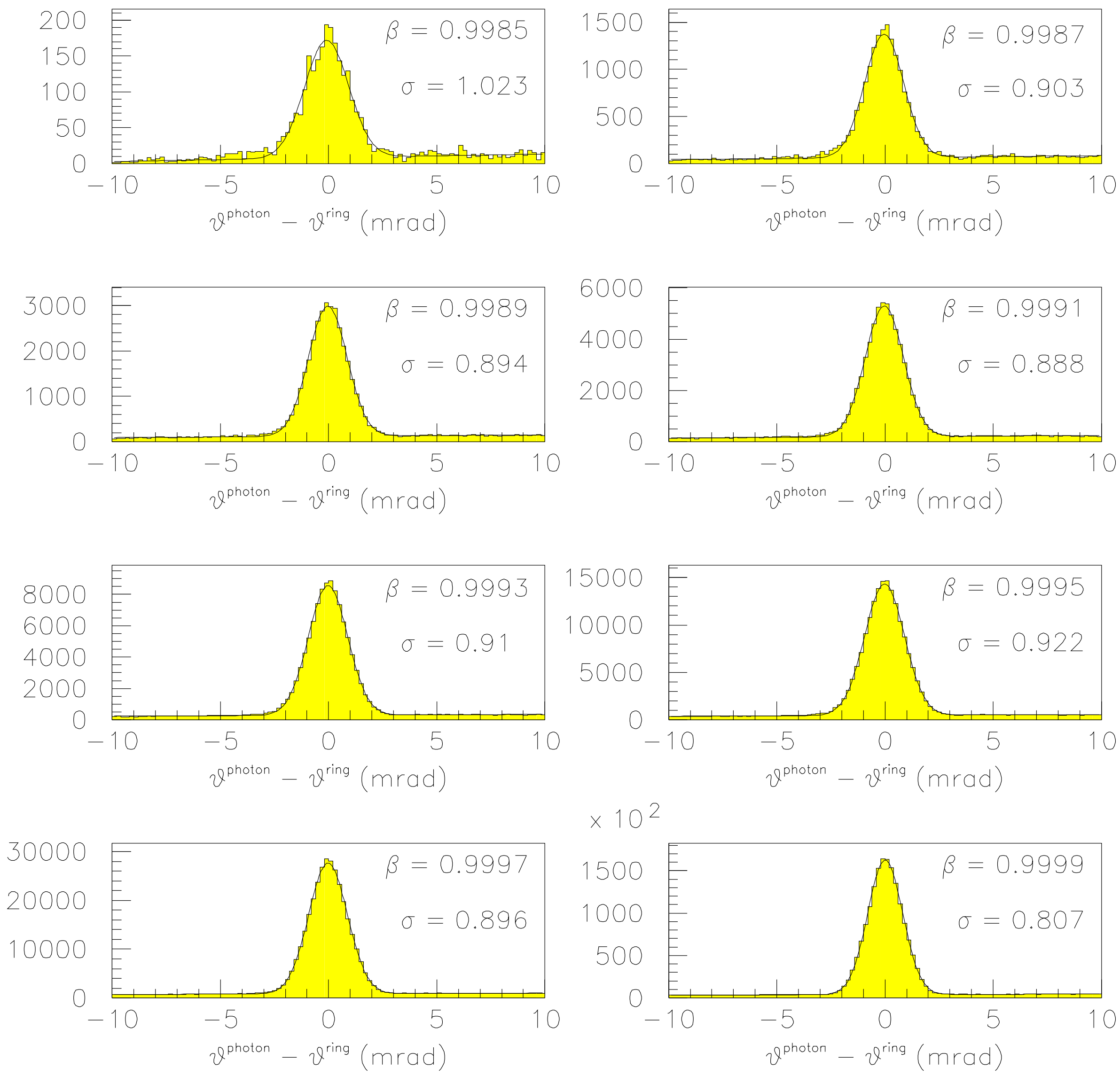

Figure 19: The same distribution as in fig.18 in bins of particle β, from threshold to 1.

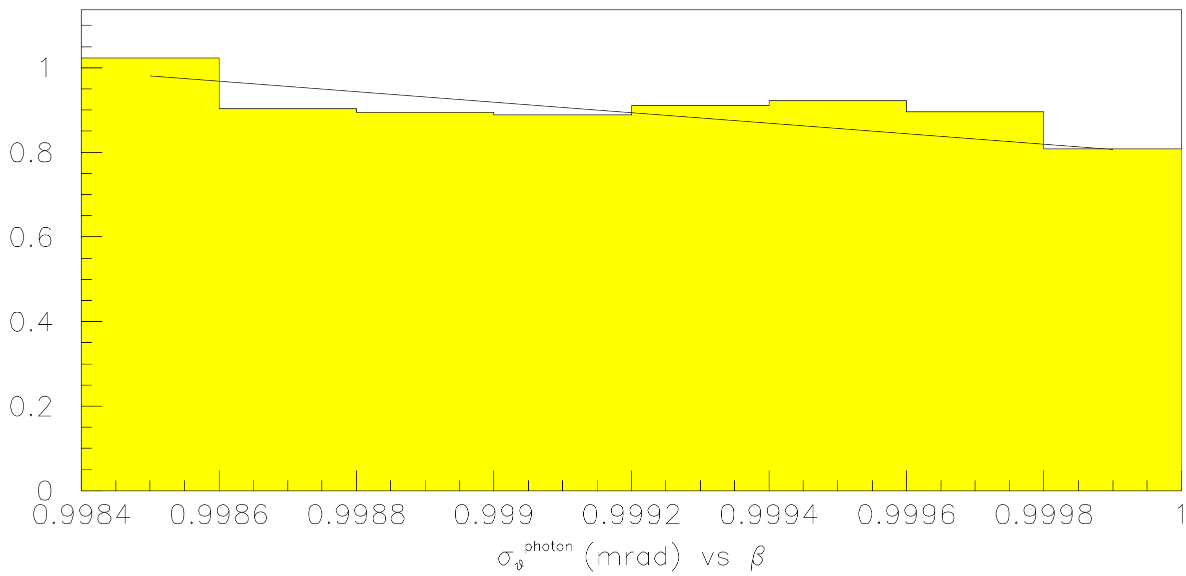

Figure 20: σ_θ^{photon} as a function of β; the fit is to the form $a + b(1 - \beta^2)$, with a = 0.8 and b = 62.; the result in almost a constant.

	μ	π	K	p
p	310	1	1	1141
K	3627	22	6250	22
π	40601	129711	48	50
μ	52916	9125	47	52

particle identification table

Figure 21: Particle mass assignments: the columns represent the particle types as indicated, known from MC input; the rows, the particle types as identified with the procedure described. Correct assignments lie along the diagonal.

	π	K	p
p			
K			
π	48068	11	15

PID, mom = 2.5

	π	K	p
p			
K		270	
π	48612	29	19

PID, mom = 7.5

	π	K	p
p			
K	8	2620	4
π	18037	5	5

PID, mom = 12.5

	π	K	p
p			230
K	2	1523	15
π	7643		9

PID, mom = 17.5

	π	K	p
p	1		427
K		826	2
π	3655		2

PID, mom = 22.5

	π	K	p
p			228
K	1	458	1
π	1911		

PID, mom = 27.5

	π	K	p
p			132
K	1	256	
π	964	1	

PID, mom = 32.5

	π	K	p
p			67
K		144	
π	465		

PID, mom = 37.5

	π	K	p
p		1	33
K	6	79	
π	215		

PID, mom = 42.5

	π	K	p
p			16
K	1	40	
π	103	1	

PID, mom = 47.5

	π	K	p
p			6
K	3	20	
π	30	1	

PID, mom = 52.5

	π	K	p
p			2
K		14	
π	8		

PID, mom = 57.5

Figure 22: Particle mass assignments for π, K and p, in momentum bins of 5.GeV/c, from 0. to 60.GeV/c.

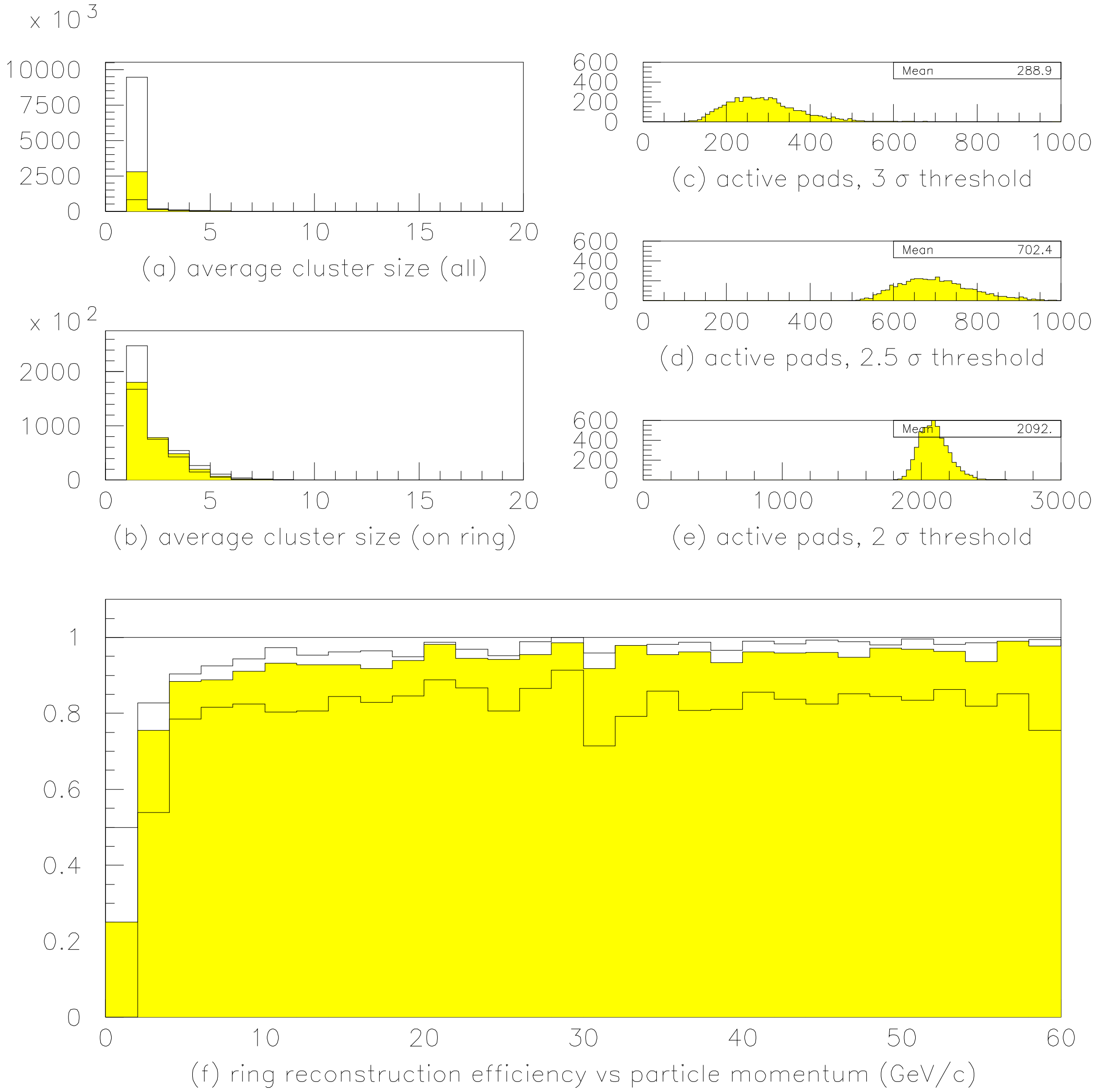

Figure 23: The average cluster size (a) and (b), the active pad distribution (c),(d) and (e) and the reconstruction efficiency as a function of the particle momentum (f) for three different settings of the pad pulse height threshold (3 σ, 2.5 σ and 2 σ).

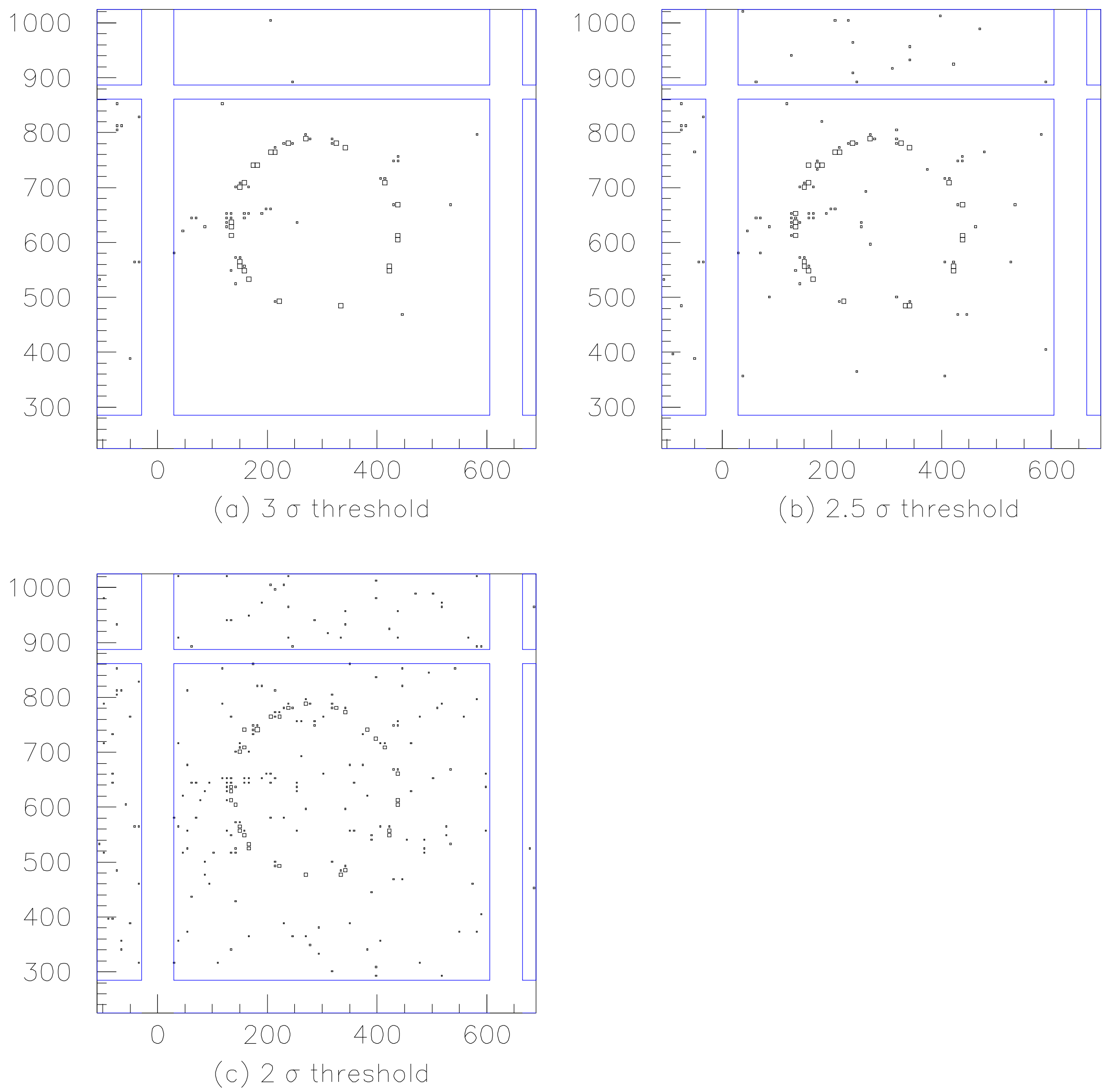

Figure 24: A visual presentation of the background density for three settings of the pad pulse height threshold, 3 σ (a), 2.5 σ (b) and 2 σ (c).

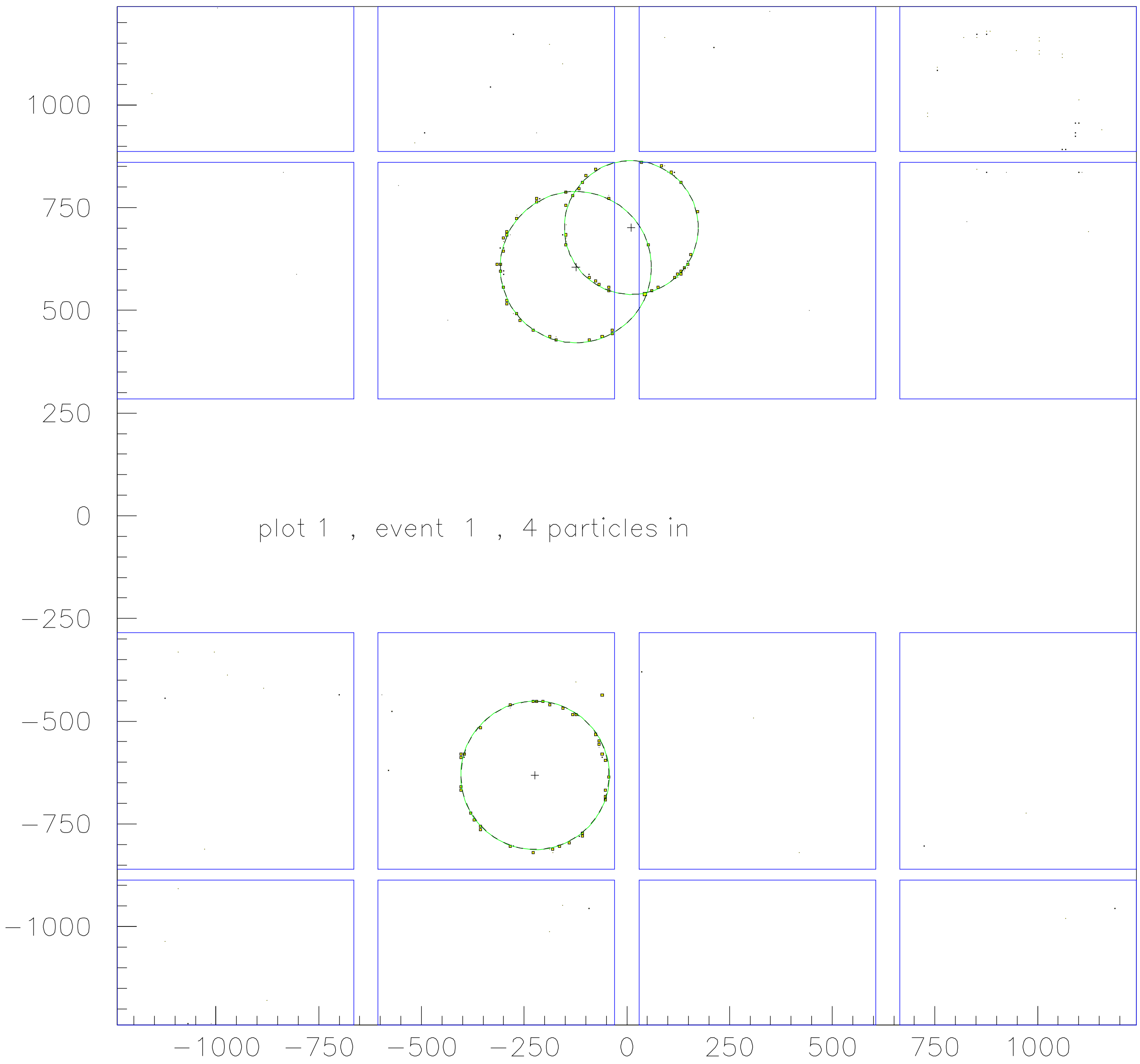

Figure 25: General display of the photon detectors, with three reconstructed *rings*. The fourth particle has not been processed for *ring* recognition.

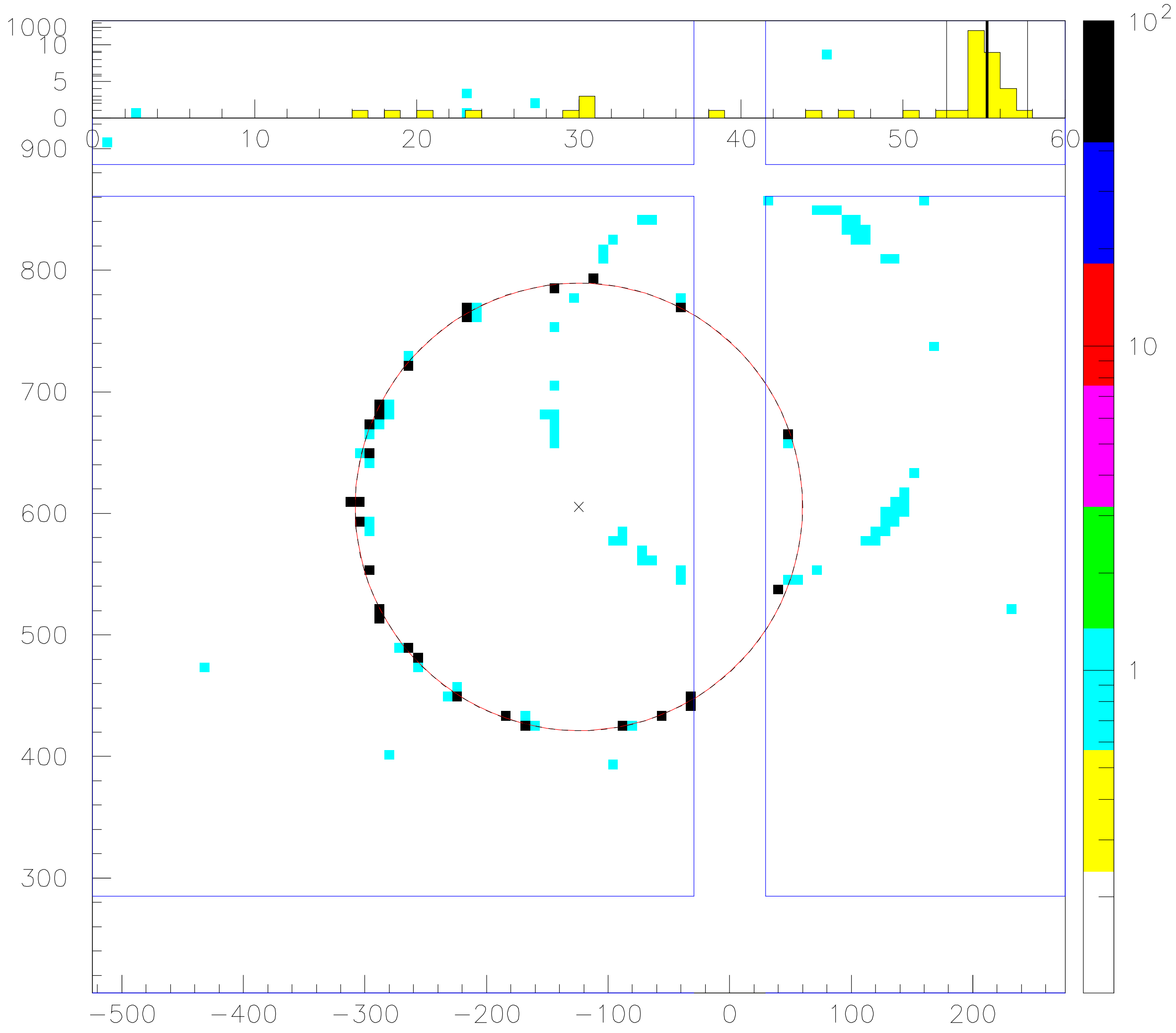

Figure 26: An elarged view of a *ring* of the previous picture; see the text for the description.

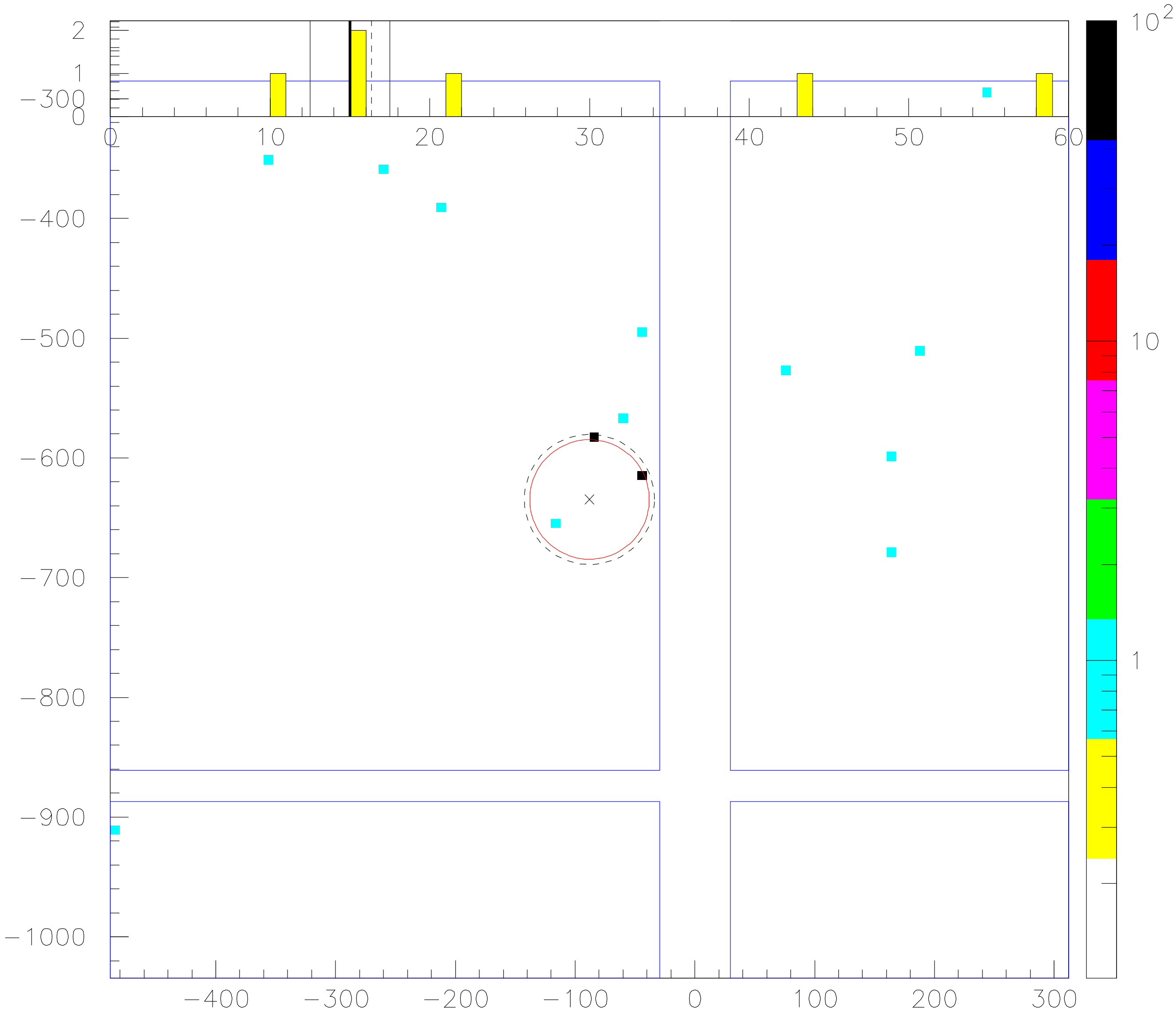

Figure 27: An elarged view of a *ring* reconstructed with only two photons.

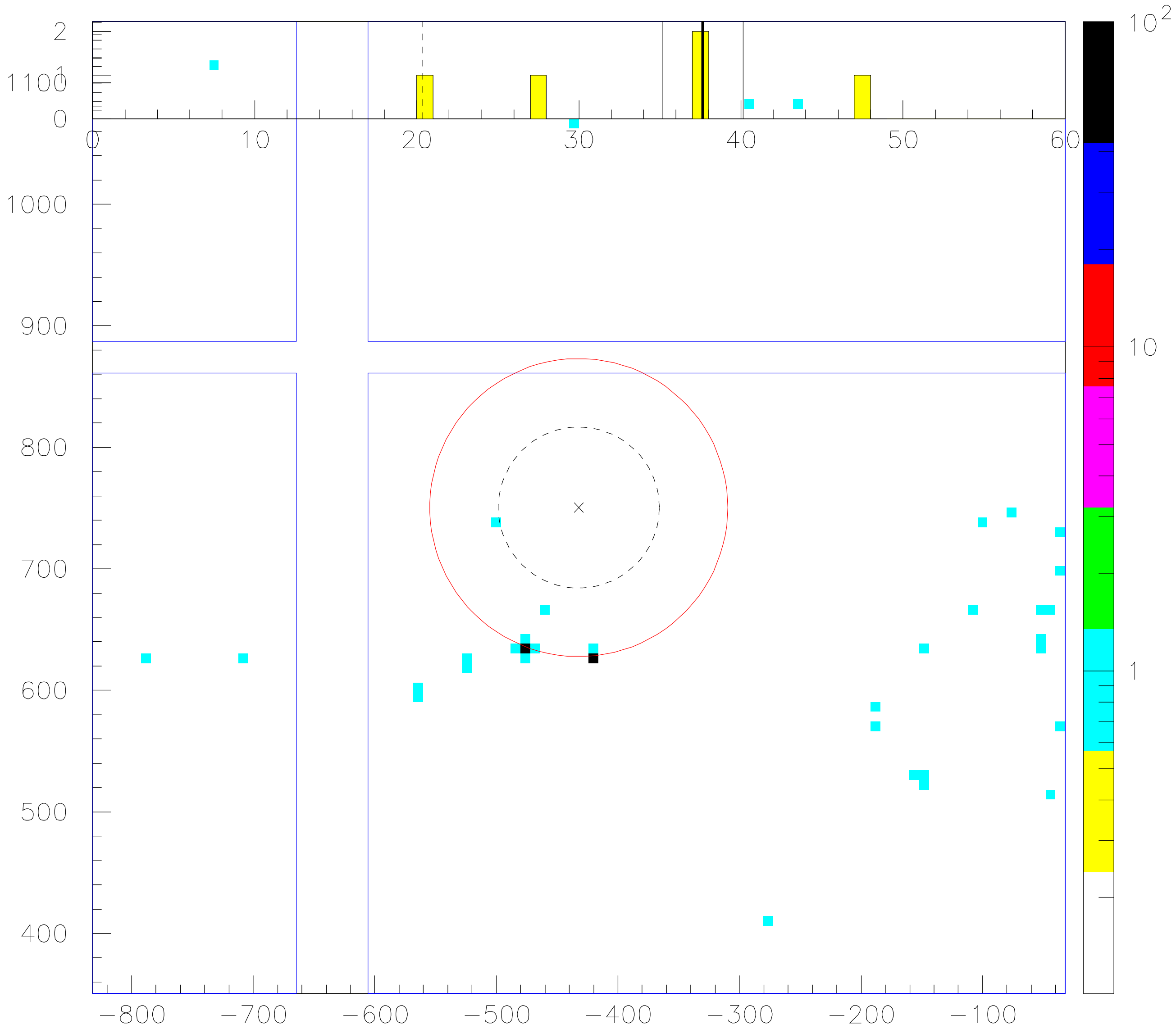

Figure 28: An exemple of a *ring* wrongly reconstructed: background photons override the only possibly good photon.

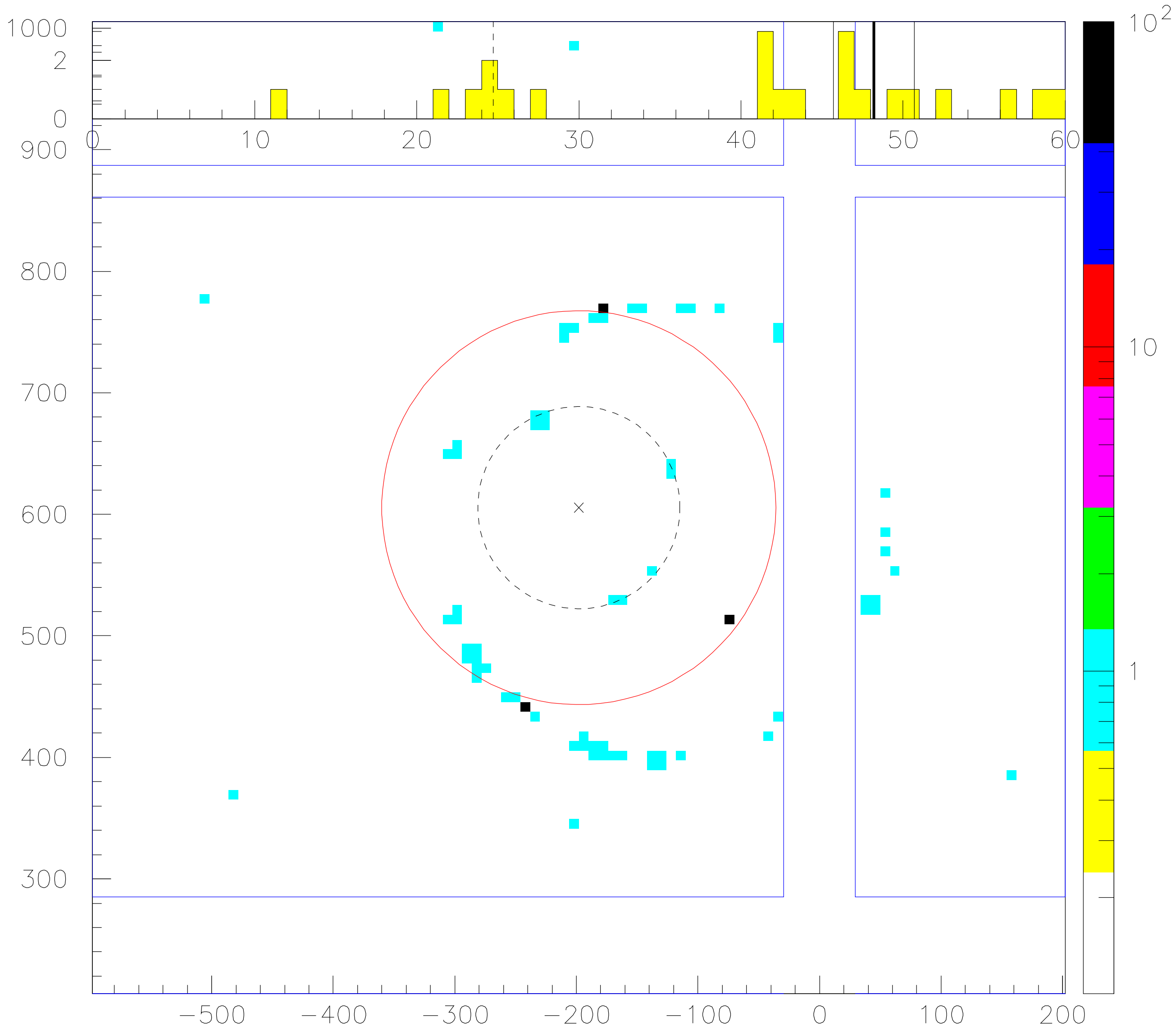

Figure 29: An example of a *ring* wrongly reconstructed because of the competition among photons belonging to two different *rings*.